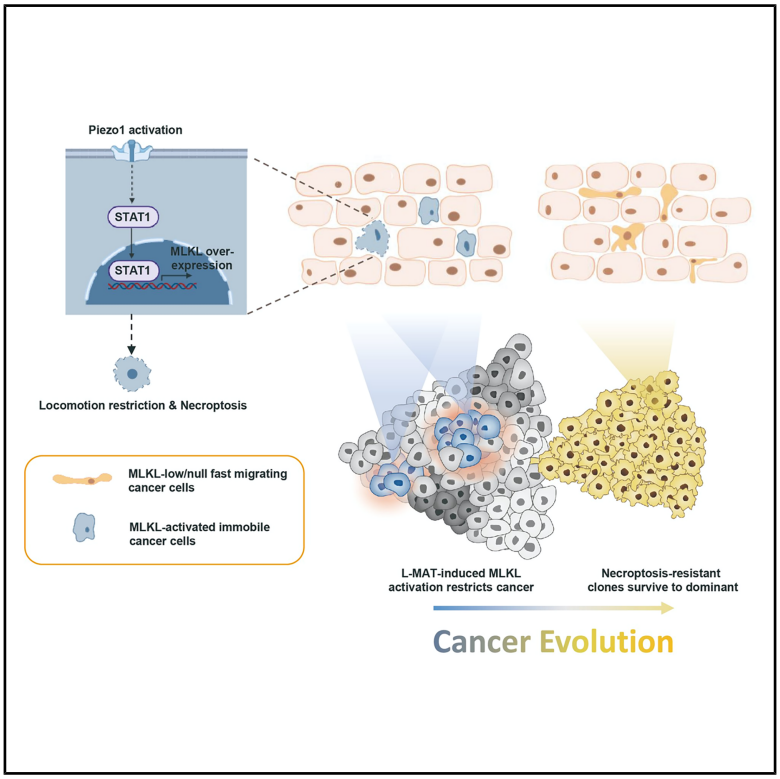
Article

Developmental Cell

Long-term confinement triggers RIPK3-independent necroptosis in amoeboid cancer cells to shape tumor evolution

Graphical abstract



Highlights

- Long-term confinement (L-MAT) triggers RIPK3-independent necroptosis in cancer cells
- PIEZO1-STAT1 drives transcriptional MLKL upregulation under L-MAT
- MLKL activation restricts amoeboid migration prior to membrane rupture during L-MAT
- MLKL-low clones escape confinement-induced death and metastasize in patients

Authors

Wei Zhang, Ya-Jun Wang, Chunman Zuo, ..., Dan Liu, Yan-Jun Liu, Liming Sun

Correspondence

Yanjun_Liu@fudan.edu.cn (Y.-J.L.), liming.sun@sibcb.ac.cn (L.S.)

In brief

Zhang et al. show that sustained confinement triggers MLKL-controlled necroptosis in MAT cells, acting as a natural barrier against invasive cancer. Cancer clones escaping this checkpoint become more aggressive, revealing an evolutionary bottleneck in cancer progression.

Zhang et al., 2026, Developmental Cell *61*, 1952–1968
October 14, 2026 © 2026 Elsevier Inc. All rights are reserved, including those for text and data mining, AI training, and similar technologies.
https://doi.org/10.1016/j.devcel.2026.09.003

CellPress

CellPress

Developmental Cell

Article

Long-term confinement triggers RIPK3-independent necroptosis in amoeboid cancer cells to shape tumor evolution

Wei Zhang,[1,7] Ya-Jun Wang,[2,7] Chunman Zuo,[3,7] Junyi He,[1] Xuying Ma,[4,5] Haoran Wu,[4,5] Bao-Qiong Lan,[2] Dehui Kong,[1] Luonan Chen,[1,6] Gang Wei,[5] Na Yang,[1] Yuandi Fu,[1] Dan Liu,[1] Yan-Jun Liu,[2,*] and Liming Sun[1,8,*]

[1]Key Laboratory of Multi-Cell Systems, Shanghai Institute of Biochemistry and Cell Biology, Center for Excellence in Molecular Cell Science, Chinese Academy of Sciences, Shanghai 200031, China

[2]Shanghai Key Laboratory of Medical Epigenetics, International Co-laboratory of Medical Epigenetics and Metabolism (Ministry of Science and Technology), Institutes of Biomedical Sciences, Fudan University, Shanghai 200032, China

[3]State Key Laboratory of Biocontrol, Innovation Center for Evolutionary Synthetic Biology, School of Life Sciences, Sun Yat-sen University, Guangzhou 510275, China

[4]Key Laboratory of Computational Biology, Shanghai Institute of Nutrition and Health, University of Chinese Academy of Sciences, Chinese Academy of Sciences, Shanghai 200031, China

[5]Key Laboratory of Molecular Virology and Immunology, Shanghai Institute of Materia Medica, Chinese Academy of Sciences, 320 Yueyang Road, Shanghai 200031, China

[6]Key Laboratory of Systems Health Science of Zhejiang Province, Hangzhou Institute for Advanced Study, University of Chinese Academy of Sciences, Hangzhou 310024, China

[7]These authors contributed equally

[8]Lead contact

*Correspondence: Yanjun_Liu@fudan.edu.cn (Y.-J.L.), liming.sun@sibcb.ac.cn (L.S.)

https://doi.org/10.1016/j.devcel.2026.09.003

SUMMARY

The mesenchymal-amoeboid transition (MAT) enhances cancer cell migration and therapy resistance during dissemination through mechanically confined spaces. Using an *in vitro* MAT induction system combining physical confinement with a non-adhesive environment to mimic interstitial migration, we introduce "long-term MAT" (L-MAT) to describe cells sustaining MAT under prolonged pressure and show that L-MAT triggers receptor-interacting protein kinase 3 (RIPK3)-independent necroptosis. Mechanistically, the PIEZO1-STAT1 axis upregulates mixed lineage kinase domain-like pseudokinase (MLKL), whose membrane accumulation drives necroptosis in cells otherwise resistant to death-receptor signaling. Before membrane rupture, L-MAT cells show progressive migration restriction; *MLKL*-knockout cells bypass this checkpoint and persist as surviving clones. Spatial transcriptomics of patient tumors shows MLKL expression correlates with PIEZO1 activation and immunogenicity in less aggressive regions, while advanced malignant and metastatic clones show reduced MLKL. These findings establish MLKL as a conditional tumor checkpoint and identify the PIEZO1-STAT1-MLKL axis as a predictive biomarker and therapeutic target.

INTRODUCTION

Cancer progression unfolds over extended timescales within a complex three-dimensional (3D) microenvironment that imposes evolving mechanical constraints. Traditional two-dimensional (2D) Petri-dish cultures do not recapitulate these features, particularly the compressive and confining stresses encountered as tumors expand. Among the cellular programs enabling dissemination, the mesenchymal-amoeboid transition (MAT) is a central driver of tumor cell migration and plasticity.[1–6] Their enhanced adaptability also allows MAT cancer cells to withstand therapeutic and immune pressures, positioning them as an evolutionary "hub" from which more aggressive, therapy-resistant clones can emerge.

Our previous work showed that strong confinement in a non-adhesive milieu reproduces key elements of MAT *in vitro*, biasing cancer cells toward a fast, amoeboid-like phenotype.[6] Notably, it is not confinement alone that replicates the *in vivo* conditions promoting MAT but rather the combination of confinement with a non-adhesive environment. This dual condition fosters the transition from a mesenchymal to an amoeboid phenotype, where the loss of adhesion facilitates rapid migration through the adoption of an amoeboid-like shape. However, how MAT cells ultimately affect cell fate and behavior over long-term monitoring, in a way that more accurately reflects long-term cancer progression *in vivo*, remains poorly understood.

Mixed lineage kinase domain-like pseudokinase (MLKL) is an endogenous membrane-breaking protein in mammalian cells,

 © 2026 Elsevier Inc.
All rights are reserved, including those for text and data mining, AI training, and similar technologies.

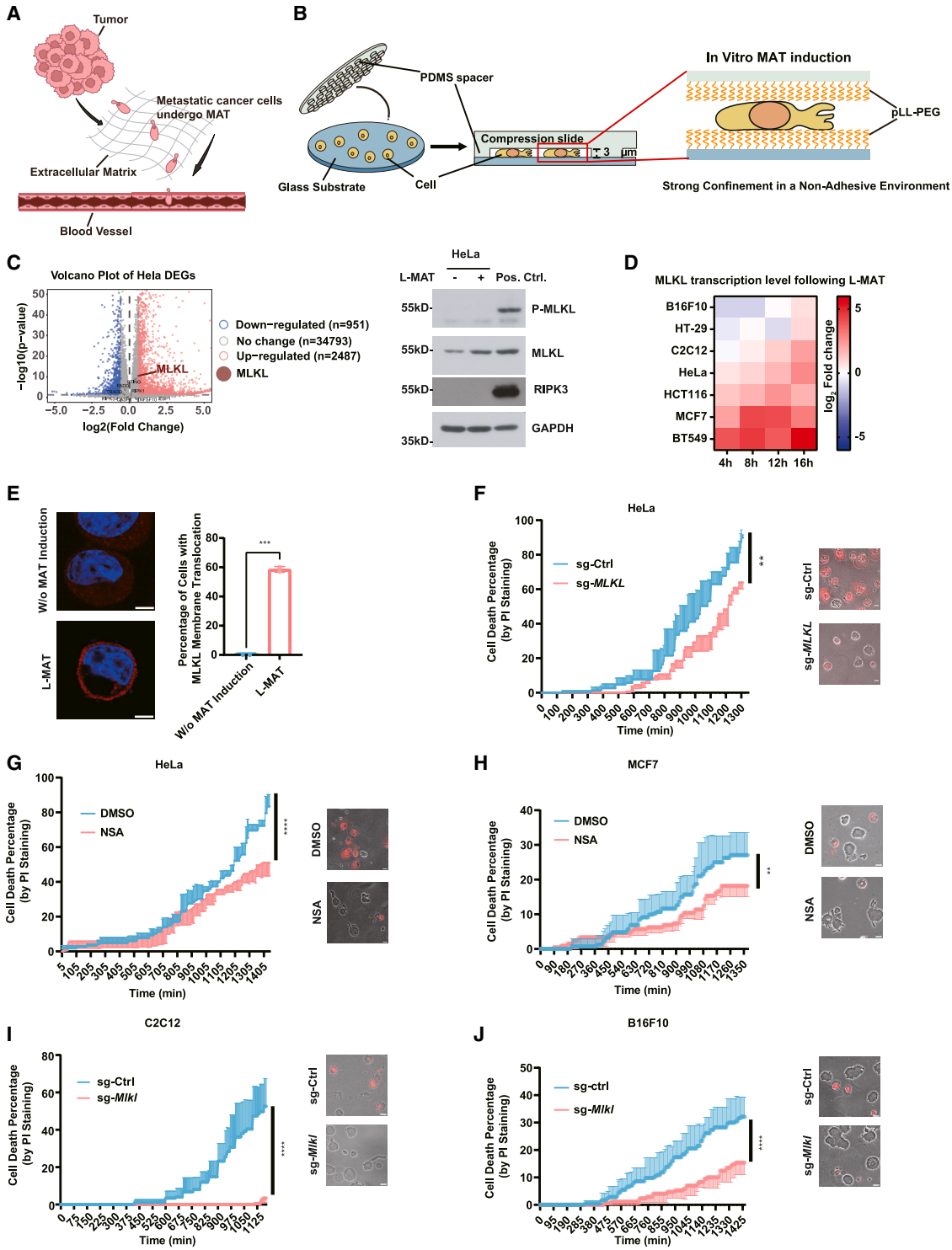


Figure 1. L-MAT triggers MLKL-dependent, RIPK3-independent necroptosis

(A) Schematic of amoeboid metastatic cancer cells undergo MAT dissemination through biological barriers such as the extracellular matrix (ECM) and blood vessel walls.

(B) Experimental setup for *in vitro* MAT induction. See STAR Methods for details.

(C) Transcriptomic profiling and necroptosis-related protein expression in HeLa cells following L-MAT induction. Left: volcano plot showing differentially expressed genes 8 h after L-MAT induction. Red and blue dots indicate significantly upregulated and downregulated genes, respectively. Necroptosis-related genes are highlighted; Right: immunoblot analysis of MLKL, p-MLKL, and RIPK3 protein levels before and after L-MAT induction. HT29 cells treated with TSZ

(legend continued on next page)

whose activation leads to membrane-lytic cell death, also known as necroptosis.[7] Canonically, MLKL activation depends on phosphorylation by the upstream kinase receptor-interacting protein kinase 3 (RIPK3) following death-receptor signaling; phosphorylated MLKL relieves autoinhibition, oligomerizes, translocates to membranes, and compromises membrane integrity.[8–13] Many human cancer cell lines, however, lack RIPK3 expression and are therefore considered resistant to death receptor-induced necroptosis.[14] This stands in contrast to the frequent observation of necrotic tumor cores in solid malignancies—including regions that appear adequately perfused—where membrane-lytic death is evident.[15–18] A central open question is whether MLKL-mediated necroptosis can arise *in vivo* without RIPK3 expression or upstream death-receptor activation.

Most necroptosis studies have been performed in 2D culture, reinforcing the view that RIPK3-deficient cancers resist TNF family-driven necroptosis. We posit that this paradigm overlooks the 3D physical context of growing tumors. Investigating how intratumoral mechanical pressure and confinement—conditions that mimic the MAT-favoring state in a strong confinement, non-adhesive assay—intersect with MLKL activation, particularly in RIPK3-deficient cancers, could reveal context-specific routes to necroptosis and expose therapeutic opportunities to modulate MLKL, constrain tumor growth, and limit dissemination.

In vivo, cancer progression is a prolonged process driven by clonal selection, where more aggressive clones with greater MAT capacity emerge and outcompete less aggressive ones.[19,20] As tumors enlarge, intratumoral pressure intensifies due to increased cellular crowding, extracellular-matrix deposition, and stromal infiltration.[21,22] Whether and how necroptosis feeds back on L-MAT under strong confinement to shape the evolutionary trajectory of tumor cells remains unknown.

Addressing this gap, here we found that MAT cancer cells exposed to prolonged confinement in a non-adhesive 3D microenvironment undergo Piezo1-driven transcriptional upregulation of MLKL, progressive restriction of migration, and ultimately RIPK3-independent necroptotic cell death. In contrast, MLKL-low cancer cells evade this death fate, retain sustained motility, and persist as surviving clones. Spatial transcriptomic analysis of breast cancer patient samples revealed a positive correlation between MLKL upregulation and local cell density in less aggressive tumor regions, as well as with tumor immunogenicity, whereas more malignant clones had escaped MLKL induction and were less sensitive to Piezo1 activation. Consistently, in advanced colorectal cancer patients with liver metastases, MLKL transcript levels were significantly lower at the metastatic front than in the matched primary tumor regions.

Our findings reveal that, in solid tumors, long-term MAT cancer cells can undergo MLKL-mediated necroptosis even in the absence of RIPK3, defining a mechanically triggered cell death modality that bypasses classical death-receptor activation. This pathway acts as a natural "braking mechanism," whereby confinement-driven MLKL activation eliminates the dangerous MAT cancer cells. However, because necroptosis preferentially removes MAT cells, clonal evolution progressively enriches for necroptosis-resistant, more aggressive clones—an evolutionary dynamic that echoes the notion that "what does not kill you makes you stronger." By directly linking cellular mechanics to cell death signaling, these results uncover a previously underappreciated layer of selection in tumor progression and open new avenues for therapeutic intervention.

RESULTS

L-MAT triggers MLKL-dependent, RIPK3-independent necroptosis

During metastatic dissemination, amoeboid cancer cells undergoing the MAT traverse biological barriers—including the extracellular matrix (ECM) and vascular walls—while experiencing substantial mechanical confinement (Figure 1A). Previous studies, including ours, have shown that short-term MAT induction (minutes to hours) is sufficient to trigger a rapid switch to amoeboid motility, thereby facilitating metastatic dissemination under confined conditions.[6,23,24] However, cancer progression unfolds over months to years under chronic mechanical constraints, and the long-term fate of MAT cells under sustained pressure remains unclear.

We therefore operationally define exposure to MAT-inducing conditions for $\geq$8 h as L-MAT ("long-term MAT"), distinguishing it from the acute short-term MAT paradigm. Using our established *in vitro* MAT induction system[6]—combining strong physical confinement with a non-adhesive environment to recapitulate migration through narrow interstitial spaces—we extended the observation window to interrogate long-term cellular fate. Wild-type HeLa cells were cultured on poly(L-lysine)-graft-poly (ethylene glycol) (PLL-PEG)-coated substrates and subjected

(TNF-α/Smac mimetic/z-VAD-FMK) undergoing canonical necroptosis were included as a positive control for RIPK3 expression and activation. GAPDH served as a loading control.

(D) Temporal dynamics of MLKL transcriptional induction across cell lines. Heat map displaying MLKL mRNA levels at indicated time points following L-MAT induction (n = 3).

(E) L-MAT triggers MLKL membrane translocation indicative of overexpression-induced activation. HeLa cells, post 13 h MAT induction. MLKL (red); DAPI (blue). Scale bar, 5 μm.

(F) CRISPR-Cas9 deletion of MLKL (LentiCRISPRv2) reduces L-MAT-induced death in HeLa cells. Left: quantification of cell death over time. Right: representative images of propidium iodide (PI)-positive cells, with PI staining shown in red indicating plasma membrane rupture. Scale bar, 20 μm (n = 136 (control) and 125 (*MLKL*-knockout) cells).

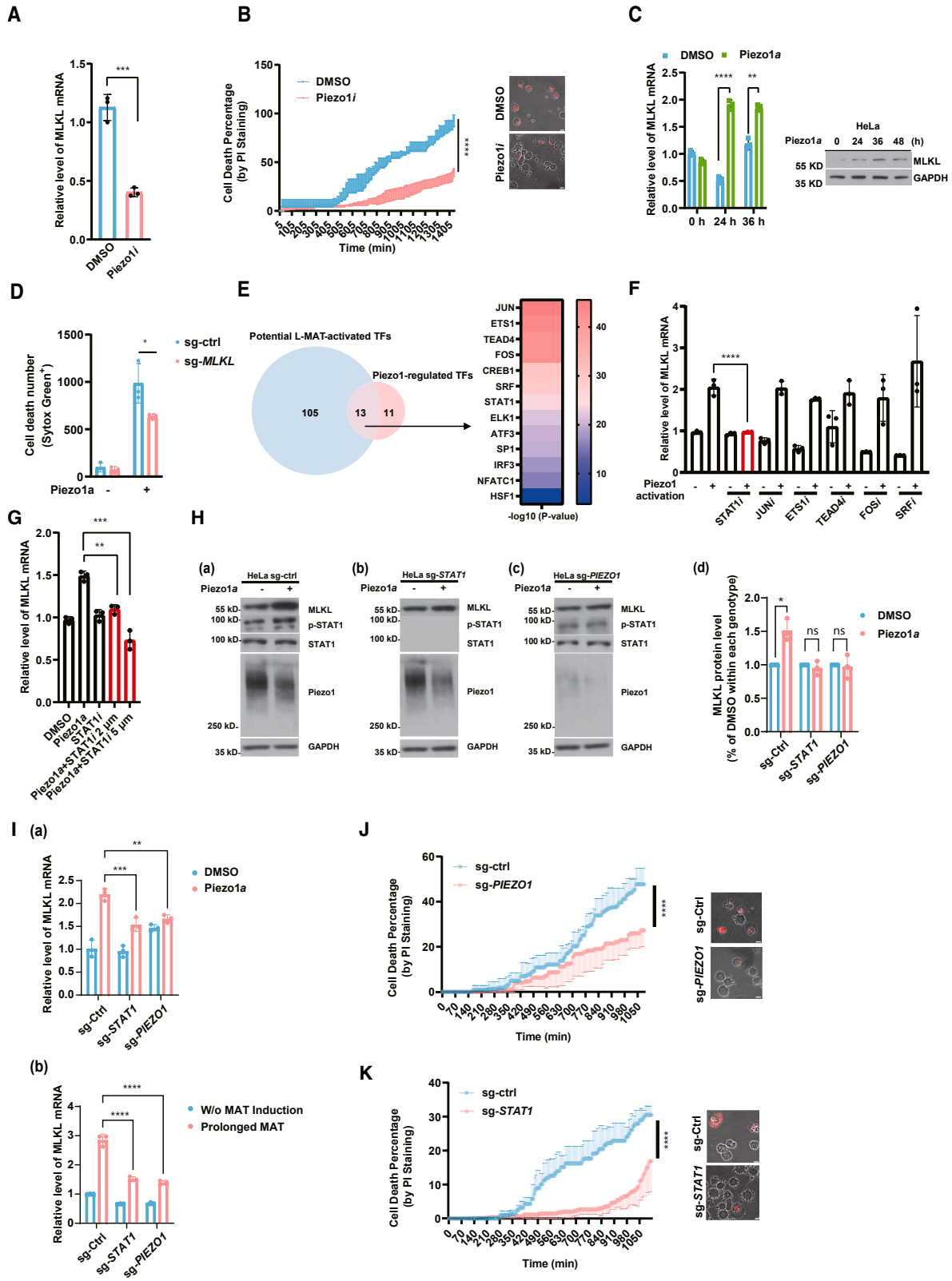
(G) The MLKL inhibitor necrosulfonamide (NSA; 1 μM) reduces L-MAT-induced death in HeLa cells. As in (F) (n = 109 [DMSO] and 122 [NSA] cells).

(H) As in (G), in MCF7 cells (n = 127 [DMSO] and 131 [NSA] cells).

(I) As in (F), in *Mlkl*-knockout C2C12 cells (n = 161 [control] and 155 [*Mlkl*-knockout] cells).

(J) As in (F), in *Mlkl*-knockout B16F10 cells.(n = 192 [control] and 166 [*Mlkl*-knockout] cells).

Bars show mean ± SD; individual dots represent single cells. Statistical analysis was performed using unpaired two-tailed Student's t test with Welch's correction. $^{**}p < 0.01$, $^{***}p < 0.001$, $^{****}p < 0.0001$. All experiments were repeated $\geq$3 independent times with consistent results; statistical analysis was conducted on pooled replicate data.



(legend on next page)

to vertical confinement (3 μm) using PDMS spacer compression slides, similarly coated to ensure complete detachment from both surfaces (Figure 1B).

Surprisingly, RNA sequencing (RNA-seq) of HeLa cells subjected to L-MAT revealed significant enrichment of the necroptosis pathway (Figure S1A)—unexpected, as HeLa cells lack RIPK3, a feature generally associated with necroptosis resistance. Among core necroptosis components, only MLKL showed robust transcriptional upregulation following L-MAT, while TNF-related apoptosis-inducing ligand (TRAIL), Fas-associated protein with death domain (FADD), TNFR1-associated death domain protein (TRADD), caspase-8, RIPK1/3, and ZBP1 remained unchanged (Figure 1C, left). Immunoblotting confirmed MLKL upregulation without detectable p-MLKL or RIPK3 (Figure 1C, right). This transcriptional induction was consistent across multiple cell lines (Figure 1D). Given that MLKL overexpression alone can induce necroptosis independent of RIPK3 —as demonstrated in Figure S2A and previous reports[10]—our findings suggest L-MAT triggers necroptosis through direct transcriptional MLKL upregulation.

Consistent with this model, L-MAT induced MLKL membrane translocation, a hallmark of MLKL activation, visualized by immunofluorescence (Figure 1E). Genetic ablation of *MLKL* via CRISPR-Cas9 significantly reduced L-MAT-induced cell death in HeLa cells (Figure 1F; knockout efficiency in Figure S1B). Pharmacological MLKL inhibition using necrosulfonamide (NSA)[7] similarly blocked L-MAT-induced death in HeLa (Figure 1G) and MCF7 cells (Figure 1H), indicating this mechanism is not cell-type specific.

Extending to murine systems, *Mlkl* knockout abolished L-MAT-induced cell death in C2C12 myoblasts (Figure 1I) and markedly reduced death in B16F10 melanoma cells (Figure 1J; knockout efficiency in Figure S1B), demonstrating that L-MAT-induced, MLKL-dependent necroptosis is conserved across species and occurs independently of RIPK3 status, as both HeLa and B16F10 cells are RIPK3 deficient.

To exclude alternative death pathways, the ROS inhibitor N-acetylcysteine (NAC) and pan-caspase inhibitor z-VAD failed to prevent L-MAT-induced death in HeLa, C2C12, and B16F10 cells (Figures S1C–S1E), confirming that death occurs via MLKL-dependent necroptosis rather than ROS-mediated damage or apoptosis.

Together, these results demonstrate that L-MAT triggers MLKL transcriptional upregulation and subsequent RIPK3-independent necroptosis, challenging the conventional paradigm that necroptosis requires upstream kinase activity. Importantly, this process is elicited by persistent physical confinement alone—not by canonical biochemical stimuli, pharmacological agents, or metabolic stressors—underscoring a decisive role for mechanical microenvironmental forces in governing cancer cell fate over evolutionary and progressive timescales.

Piezo1-STAT1 signaling drives MLKL upregulation following L-MAT

Having established that L-MAT triggers MLKL-dependent necroptosis in RIPK3-null cells, we next sought to understand the mechanistic basis for this RIPK3-independent process. Ectopic MLKL expression in HEK293T cells induced dose-dependent cell death independent of RIPK3 (Figure S2A), indicating elevated MLKL levels alone are sufficient to trigger necroptosis, bypassing RIPK3-mediated activation. We therefore focused on identifying the mechanosensitive signaling pathway responsible for L-MAT-induced MLKL transcriptional upregulation.

Figure 2. Piezo1-STAT1 signaling drives MLKL upregulation following L-MAT induction

(A) The Piezo1 inhibitor GsMTx4 (10 μM; referred to as Piezo1*i*) reduces L-MAT-induced MLKL upregulation in HeLa cells ($n = 3$).

(B) Piezo1 inhibition prevents L-MAT-induced cell death. Time-course analysis of cell death in HeLa cells treated with GsMTx4 (10 μM). Representative images show PI-positive cells indicating plasma membrane rupture. Scale bar, 20 μm ($n = 84$ [control] and 106 [GsMTx4] cells).

(C) The Piezo1 activator Yoda1 (5 μM; referred to as Piezo1*a*) induces MLKL upregulation in HeLa cells in 2D condition ($n = 3$).

(D) Piezo1 activation induces MLKL-dependent necroptosis in 2D condition. Control (sg-Ctrl) or *MLKL*-knockout (sg-*MLKL*) HeLa cells were treated with Yoda1 (1 μM). Cell death was quantified after 72 h using Sytox Green staining ($n = 3$).

(E) Candidate transcription factors (TFs) mediating MLKL upregulation: TFs predicted from the L-MAT RNA-seq data (Figure 1C) using ChEA3 were intersected with reported Piezo1-regulated TFs; heat map shows ranking by *p* value.

(F) TF screening for Piezo1-mediated MLKL upregulation in 2D condition in HeLa cells. TF inhibitors: signal transducer and activator of transcription 1 (STAT1) (fludarabine, 5 μM), Jun proto-oncogene, AP-1 transcription factor subunit (JUN) (bentamapimod, 3 μM), ETS proto-oncogene 1, transcription factor (ETS1) (YK-4-279, 1 μM), TEA domain transcription factor 4 (TEAD4) (YAP/TAZ inhibitor-1, 3 μM), Fos proto-oncogene, AP-1 transcription factor subunit (FOS) (praeruptorin A, 10 μM), and serum response factor (SRF) (CCG-1423, 10 μM). MLKL mRNA levels were quantified by RT-qPCR ($n = 3$).

(G) STAT1 inhibition reduces Yoda1-induced MLKL upregulation in a dose-dependent manner in 2D condition. HeLa cells were treated with Yoda1 in combination with increasing concentrations of the STAT1 inhibitor fludarabine. MLKL mRNA levels were quantified by RT-qPCR ($n = 3$).

(H) PIEZO1 activation induces MLKL protein upregulation in 2D condition. Immunoblot analysis of PIEZO1, phospho-STAT1, STAT1, and MLKL protein expression in control, *PIEZO1*-knockout, and *STAT1*-knockout HeLa cells following Yoda1 or DMSO treatment. As each genotype was analyzed on a separate gel, MLKL protein levels were normalized to the DMSO-treated group within each respective gel to account for inter-gel variability; statistical comparisons were therefore performed within each genotype ($n = 3$).

(I) Yoda1- or L-MAT-induced MLKL transcriptional upregulation requires *PIEZO1* and *STAT1*. *MLKL* mRNA levels were quantified by RT-qPCR in control, *PIEZO1*-knockout, and *STAT1*-knockout HeLa cells following Yoda1 treatment in 2D condition (a) or L-MAT induction (b). All samples were measured in one batch against a shared reference (sg-Ctrl with DMSO in [a]; sg-Ctrl without MAT in [b]), allowing comparison across genotypes ($n = 3$).

(J and K) L-MAT induces cell death in a Piezo1-STAT1-dependent manner. Time-course analysis of cell death in control, *PIEZO1*-knockout (J), or *STAT1*-knockout (K) HeLa cells under MAT induction. Representative images show PI-positive cells indicating plasma membrane rupture. Scale bar, 20 μm. ($n = 146$ [sg-Ctrl] and 156 [PIEZO1-knockout] cells in J; $n = 278$ [sg-Ctrl] and 810 [STAT1-knockout] cells in K.)

Bars depict mean ± SD; dots represent individual replicates or single cells, depending on assay. Statistical analysis was performed using an unpaired two-tailed Student's *t* test with Welch's correction for comparisons in (A), two-way ANOVA followed by Sidak's multiple comparisons test for (B)–(D), (F), (G), (Ia), (Ib), (J), and (K), and one-sample *t* test comparing normalized values against a theoretical value of 1 for (Hd). $^{*}p < 0.05$, $^{**}p < 0.01$, $^{***}p < 0.001$, $^{****}p < 0.0001$, ns, not significant. All experiments were repeated at least three independent times with consistent results; statistics were calculated from pooled replicate data.

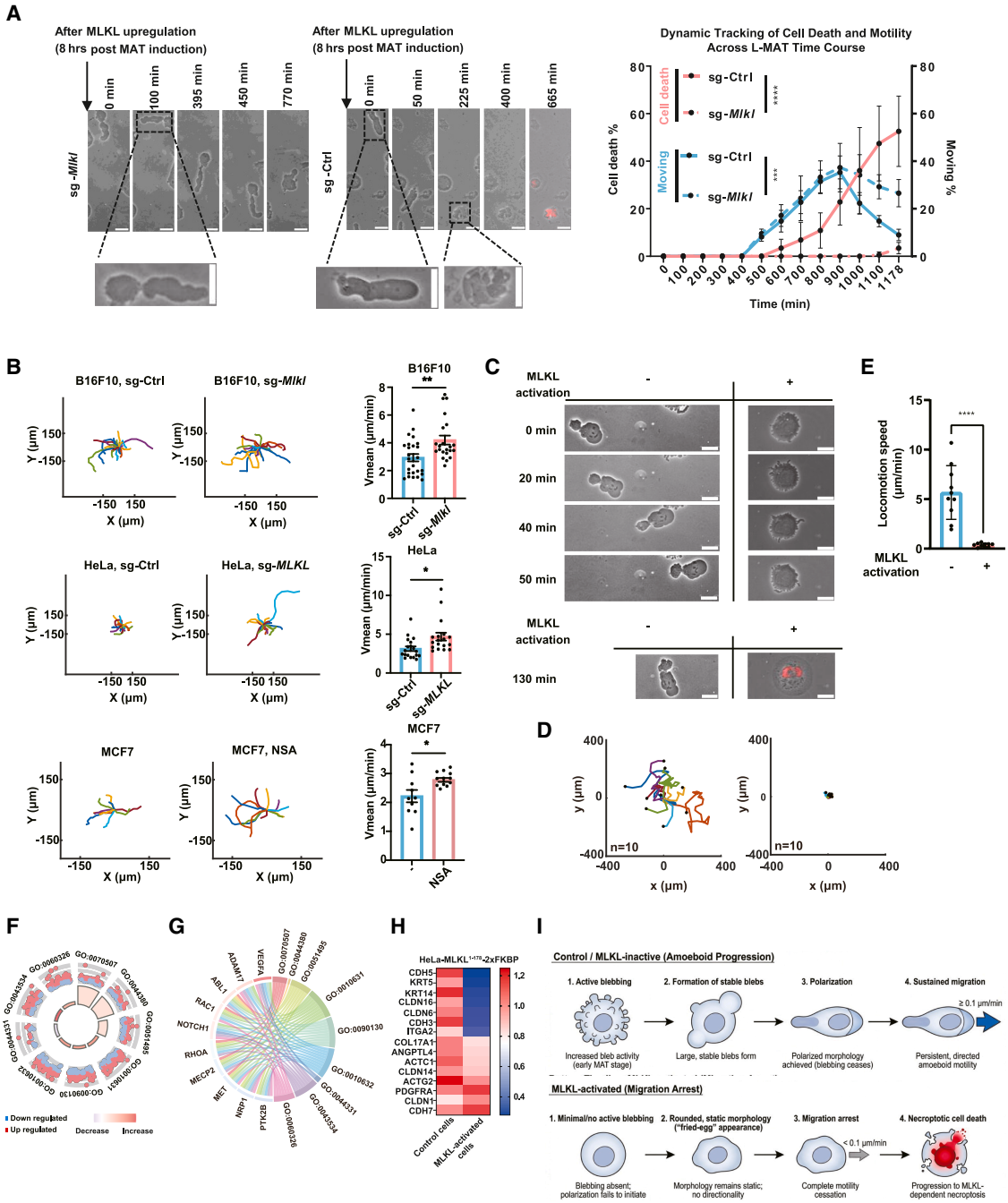


Figure 3. MLKL activation restricts amoeboid migration in MAT cells before culminating in final death

(A) L-MAT reduces amoeboid motility in control but not MLKL-knockout cells. Real-time tracking of cell movement in C2C12-sg-Ctrl (control) and C2C12-sg-*Mlkl* (MLKL-knockout) cells was performed 8 h after L-MAT induction, coinciding with the onset of MLKL transcriptional upregulation (see Figure 1C). Left: representative images of amoeboid migration for each condition. Right: time-course quantification showing the proportion of motile cells (blue) and dead cells (pink). Cells were classified as motile if displacement was ≥0.1 μm/min (blue lines; A, right) or non-motile if displacement was <0.1 μm/min. The *y* axis indicates the percentage of cells meeting the motility criterion at each time point ($n = 175$ [sg-ctrl] and 175 [*MLKL*-knockout] cells for cell death; $n = 110$ [sg-ctrl] and 109 [*MLKL*-knockout] cells for motility).

(B) *MLKL* knockout prolongs amoeboid migration capacity under L-MAT across multiple cell lines. Left: representative migration trajectories of indicated cells under confinement. Starting positions were registered to the center of each plot. Right: quantification of mean migration speed. Analyzed sample numbers: B16F10, $n = 25$ (sg-ctrl) and 22 (sg-*Mlkl*); HeLa, $n = 25$ (sg-ctrl) and 22 (sg-*MLKL*); MCF-7, $n = 10$ (ctrl) and 12 (NSA).

(C) Representative migration behavior of cells with and without MLKL activation under MAT conditions. Cells expressing MLKL (1–178) fused to tandem FKBP (F36V) domains were treated with the dimerizer AP20187 to induce MLKL oligomerization and activation. Plasma membrane rupture was visualized by PI staining (bottom). Scale bar, 20 μm.

(legend continued on next page)

Mechanosensitive ion channels are prime candidates for transducing physical cues from L-MAT conditions into intracellular signaling cascades.[25,26] To systematically identify which mechanosensor mediates L-MAT-induced MLKL upregulation, we reanalyzed publicly available transcriptomic datasets. Modulation of TRPV4, TRPM7, NHE1, or AQP5 through pharmacological inhibition, knockdown, or knockout did not consistently affect MLKL transcription (Figures S3A–S3D). RNA-seq analysis revealed that PIEZO2 and TRPV4 are minimally expressed across our experimental cell lines (Figure S2B, accession number GEO: GSE328536), while PIEZO1 was robustly expressed. Previous studies established that mechanical confinement elicits PIEZO1-dependent Ca^{2+} influx,[27] supporting PIEZO1 as the primary mechanosensor under confined conditions.

To directly test whether Piezo1 mediates L-MAT-induced MLKL upregulation, we employed grammostola spatulata mechanotoxin 4 (GsMTx4), a peptide toxin that specifically inhibits Piezo1.[28] GsMTx4 treatment (labeled "Piezo1*i*") blocked L-MAT-induced MLKL transcriptional upregulation in HeLa cells (Figure 2A) and reduced L-MAT-induced cell death (Figure 2B).

Conversely, Yoda1, a Piezo1 agonist (labeled "Piezo1*a*"), induced time-dependent MLKL transcriptional and protein upregulation (Figure 2C). High-dose Yoda1 triggered necroptotic cell death in control HeLa cells, while MLKL-knockout cells were protected (Figure 2D), demonstrating Piezo1 activation is both necessary and sufficient for MLKL-dependent necroptosis.

Next, we sought to identify the transcription factor(s) downstream of Piezo1. Using the ChEA3 database, we analyzed transcription factors regulating differentially expressed genes in HeLa cells under L-MAT (RNA-seq from Figure 1C, GEO: GSE328527). Intersecting these with known Piezo1-regulated transcription factors identified 13 candidates enriched in both L-MAT and Piezo1-activation conditions (Figure 2E).

We conducted pharmacological screening of HeLa cells treated with Yoda1 plus inhibitors targeting STAT1 (fludarabine, 5 μM), JUN (bentamapimod, 3 μM), ETS1 (YK-4-279, 1 μM), TEAD4 (YAP/TAZ inhibitor-1, 3 μM), FOS (praeruptorin A, 10 μM), and SRF (CCG-1423, 10 μM). We excluded CREB1 from testing, as it has been previously reported to inhibit MLKL expression.[29] Only fludarabine, a STAT1 inhibitor, specifically reduced Yoda1-induced MLKL transcriptional upregulation in a dose-dependent manner (Figures 2F and 2G).

To genetically validate this pathway, we generated *PIEZO1*-knockout and *STAT1*-knockout HeLa cells (Figures S2C and S2D). Both knockouts significantly reduced Yoda1- and L-MAT-induced MLKL transcription (Figure 2I) and protein levels (Figure 2H).

We next examined whether the Piezo1-STAT1 pathway is required for L-MAT-induced cell death. Genetic ablation of either *PIEZO1* or *STAT1* significantly reduced L-MAT-induced cell death in HeLa cells (Figures 2J and 2K). In murine C2C12 myoblasts and B16F10 melanoma cells, *Piezo1* or *Stat1* knockout abrogated L-MAT-induced MLKL upregulation (Figure S2E) and reduced cell death (Figures S2F and S2G). Consistent with Ca^{2+} signaling downstream of PIEZO1,[30–33] BAPTA-AM chelation attenuated L-MAT-induced STAT1 phosphorylation and MLKL upregulation (Figure S2H).

These findings establish that L-MAT triggers MLKL transcriptional upregulation through the Piezo1-STAT1 axis. By elevating MLKL above a critical threshold, this mechanotransduction pathway bypasses RIPK3 requirement, enabling RIPK3-independent necroptosis in confined cancer cells.

MLKL activation restricts amoeboid migration in MAT cells before culminating in final death

Fast amoeboid migration is the hallmark of confinement-induced MAT, captured by our *in vitro* MAT induction system.[6,23,24] Surprisingly, before the final necroptotic cell death described above, we observed striking differences in amoeboid migration capacity between wild-type and *MLKL*-knockout cells. While both cell types initially transformed and migrated efficiently under MAT conditions, their behaviors diverged after 8 h: wild-type cells—exhibiting MLKL upregulation (Figures 1C and 1D)—progressively lost migratory capacity and succumbed to necroptosis, whereas MLKL-knockout cells retained motility throughout (Figure 3A; Videos S1–S4). This pattern was consistent across multiple cell lines (Figures 3B and S1B).

These observations suggest a two-phase MAT response: an early MLKL-independent transition to fast amoeboid migration, followed by progressive restriction as MLKL expression increases, culminating in cellular paralysis and necroptotic death.

(D) Migration trajectories of cells without (left) or with (right) MLKL activation, as shown in (C). $n = 10$ cells per condition.

(E) Quantification of mean migration speed of cells as shown in (C). $n = 10$ per condition.

(F) GO enrichment analysis reveals activation of adhesion and migration pathways following L-MAT. Circle plot displays enriched GO biological processes related to cell adhesion, migration, and cytoskeleton organization in HeLa cells. Inner ring colors indicate *Z* scores (activation or suppression); outer dots represent $\log_2$ fold change (logFC) of contributing genes. Several pathways, including microtubule cytoskeleton regulation (GO:0070507, GO:0044380, and GO:0051495) and cell migration (GO:0010631, GO:0090130, GO:0010632, and GO:0043534), showed overall activation.

(G) Gene-pathway chord diagram of adhesion and migration-related GO terms in L-MAT-treated HeLa cells. Chord plot illustrates connections between key genes and enriched GO biological processes. The width of each pathway sector reflects the number of contributing genes; colored ribbons represent gene–process associations.

(H) RT-qPCR analysis of migration-related gene expression in cells with or without dimerization-induced MLKL activation (±AP20187) under MAT conditions. MLKL activation significantly reduced transcription of genes associated with cell migration.

(I) Schematic summary of morphological transitions under MAT induction in MLKL-inactive control cells (top) versus MLKL-activated cells (bottom). Control cells progress from early active blebbing to stable bleb formation, followed by polarization (elongated morphology with a defined uropod; blebbing ceases) and sustained, directed amoeboid migration. In contrast, MLKL-activated cells exhibit minimal or absent blebbing, fail to polarize, adopt a rounded, static "fried egg" morphology, undergo migration arrest, and ultimately progress to necroptotic cell death (PI^+). Blue arrows denote motile cells, and gray arrows indicate non-motile cells.

Bars indicate mean ± SD; individual dots represent each tracked cell or biological replicate as appropriate. Statistical analysis was performed using unpaired two-tailed Student's *t* test with Welch's correction. $^*p < 0.05$, $^{**}p < 0.01$, $^{***}p < 0.001$, $^{****}p < 0.0001$, ns, not significant. All experiments repeated at least three independent times with consistent results; statistics calculated from pooled replicate data.

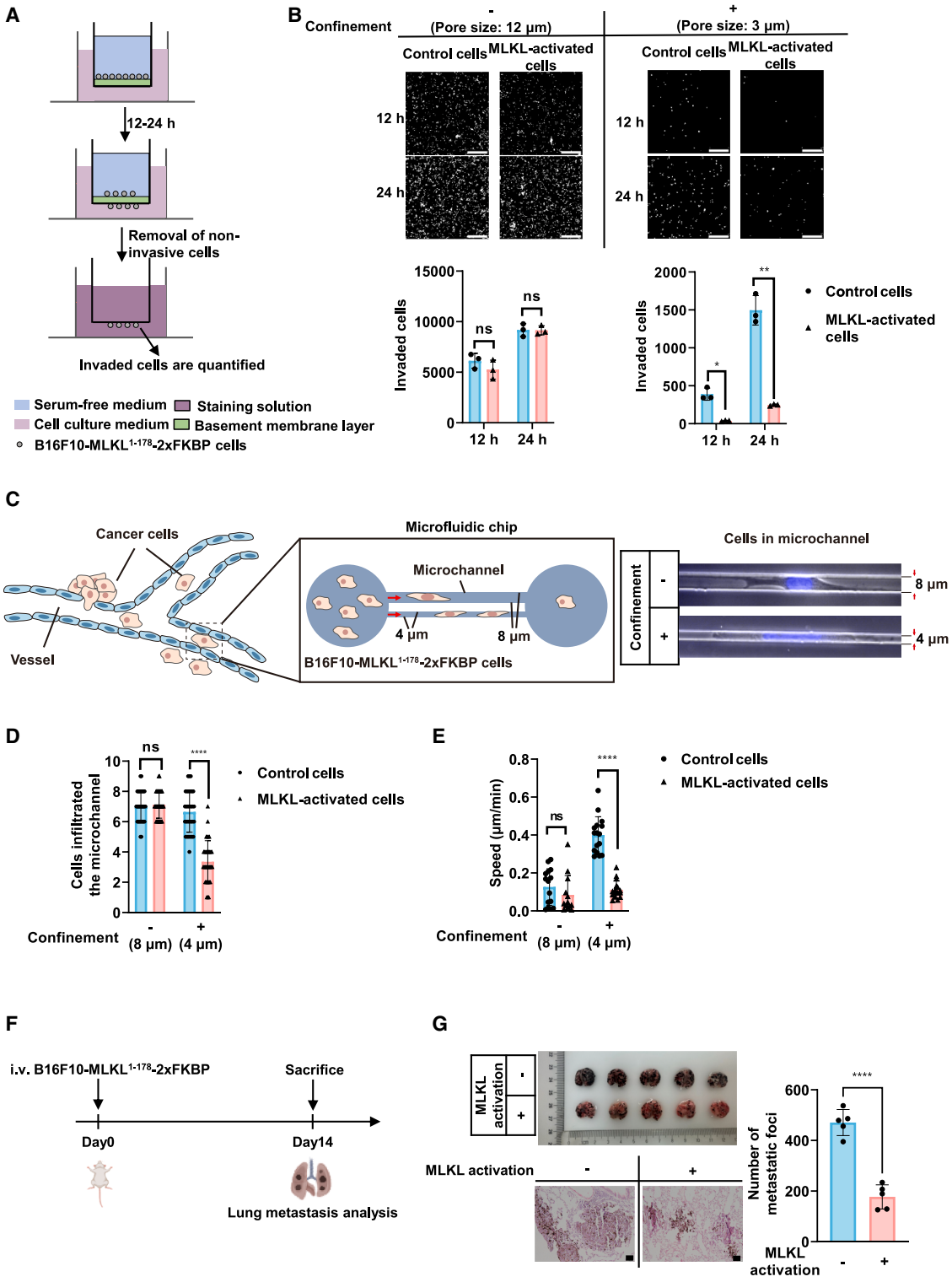


Figure 4. MLKL activation reduces cancer cell metastatic dissemination

(A) Schematic of transwell migration assay for B16F10 cells with or without MLKL activation. MLKL activation in B16F10-MLKL(1–178)-2×FKBP cells was described in Figure 3. Migrated cells were quantified by counting Hoechst-stained nuclei (10 μg/mL).

(B) Transwell migration of B16F10 cells through confined filters to mimic MAT induction. Cells with or without MLKL activation were allowed to migrate through 3 μm (confined) or 12 μm (non-confined) pore-sized filters. Upper: representative images of Hoechst-stained migrated cells. Lower: quantification of migrated cell numbers. Scale bar, 500 μm. *n* = 3 per condition.

(legend continued on next page)

Importantly, the migratory defect precedes rather than results from membrane damage. Live-cell imaging (Figure 3A) shows motility loss shortly after MLKL upregulation onset (8 h post-L-MAT), while propidium iodide (PI) uptake occurs ~4.6 h later. Control cells ceased migrating well before PI positivity, whereas Mlkl-knockout cells remained motile throughout. In our inducible MLKL activation system (Figure 3C), MLKL activation rapidly abolished migration, while PI uptake followed ~130 min later, confirming that impaired migration is not secondary to membrane disruption.

To directly compare locomotion with and without MLKL activation, we employed the 2×FKBP system, fusing tandem FKBP(F36V) dimerization domains to human MLKL(1–178). AP20187 addition triggered MLKL oligomerization and membrane translocation (Figures S4A and S4B). To prevent immediate cell death, we implemented a washout strategy using the dimerizer competitor tacrolimus to halt further MLKL activation,[34] allowing migration monitoring in MLKL-activated survivor cells under MAT induction (Figure 3C).

Under MAT conditions, non-activated control cells exhibited active blebbing followed by stabilization into a polarized, elongated morphology enabling rapid migration. MLKL activation drastically disrupted this process: cells showed reduced blebbing (Figure S4C), loss of cortical actin retrograde flow by total internal reflection fluorescence (TIRF) microscopy (Figure S4D; Video S7), and failed front-rear polarization, adopting an unpolarized "fried egg" morphology (Figure S4E; Video S5). Non-activated cells achieved fast amoeboid migration while MLKL-activated cells remained immobile (Figures 3C–3E; Video S6).

Transcriptomic analysis of L-MAT-treated HeLa cells revealed enrichment of migration and cytoskeleton-related pathways (Figures 3F and 3G), and RT-qPCR confirmed that MLKL activation significantly reduced transcription of migration-related genes (Figure 3H), indicating transcriptional reprogramming that restricts migratory capacity.

Prolonged MAT established persistent directional retrograde actin flow—the primary mechanical engine of confined amoeboid migration[6,23,24,35]—which MLKL activation abolished alongside cortical polarity. Together, MLKL restricts amoeboid migration through dual mechanisms: disruption of cortical actin dynamics and transcriptional repression of migration-associated genes, ultimately culminating in cell death under sustained MAT (Figure 3I).

MLKL activation reduces cancer cell metastatic dissemination

Having established that MLKL activation restricts amoeboid migration *in vitro*, we next investigated whether this migration-suppressive effect translates into reduced metastatic potential in physiologically relevant contexts. Confinement is a key factor that induces fast amoeboid migration, enabling cancer cells to squeeze through physical barriers such as blood vessel walls and tissue interstitial spaces during metastatic dissemination.[36,37] To investigate how MLKL activation affects cancer cell migration under confinement, we designed three experimental systems with increasing levels of physiological complexity.

First, we performed a transwell migration assay to assess the migration capacity of MLKL-activated B16F10 melanoma cells (Figure 4A). B16F10 cells stably expressing MLKL(1–178)-2×FKBP were treated with dimerizer to induce MLKL activation, followed by tacrolimus washout to halt further activation and allow cell survival (Figures S5A–S5B). Microporous membranes with different pore sizes were used to evaluate migration under varying degrees of confinement. B16F10 cells, which are approximately 15–20 μm in diameter, were placed in transwells with either 3 μm (confined) or 12 μm (non-confined) pore sizes. In the absence of strong confinement (12 μm pores), no significant difference in migration was observed between MLKL-activated and non-activated cells (Figure 4B, left). However, under confined conditions (3 μm pores), MLKL-activated cells exhibited significantly reduced migration compared with non-activated cells (Figure 4B, right).

Next, we developed a biomimetic microfluidic chip model designed to simulate cancer cell migration across tight vascular barriers during metastasis (Figure 4C). Tumor cells typically disseminate through blood vessels, where they must navigate confined spaces such as capillaries (5–10 μm in diameter).[38] Microchannels of 4 μm (confined) and 8 μm (non-confined) in width were used to mimic these physiological constraints. In the 8 μm microchannels, both MLKL-activated and non-activated B16F10 cells exhibited similar migration abilities. However, in the more confined 4 μm microchannels, MLKL-activated cells were significantly less likely to enter the channels compared with non-activated cells (Figure 4D). Furthermore, MLKL-activated cells migrated at a significantly slower speed than non-activated cells in the 4 μm microchannels (Figure 4E), with many MLKL-activated cells stalling in place rather than migrating distally (Video S8).

(C) Schematic of confined microfluidic chip assay designed to mimic cancer cell migration across tight vascular barriers during metastasis. B16F10 cells with or without MLKL activation were subjected to migration through 4 μm (confined) or 8 μm (non-confined) microchannels.

(D) MLKL activation reduces cancer cell entry into confined microchannels. Quantification of B16F10 cells that migrated into confined microchannels with or without MLKL activation. $n = 33$ channels per condition.

(E) MLKL activation reduces cancer cell migration speed in confined microchannels. Quantification of migration speeds of B16F10 cells with or without MLKL activation through 4 or 8 μm microchannels. $n = 15$ (non-activated, 8 μm), $n = 16$ (non-activated, 4 μm), $n = 13$ (MLKL-activated, 8 μm), and $n = 15$ (MLKL-activated, 4 μm).

(F) Schematic of *in vivo* lung metastasis model. B16F10 cells with or without MLKL activation were injected into mice, and lung metastasis was assessed 14 days post-injection.

(G) MLKL activation reduces lung metastatic colonization. Upper left: representative images of mouse lungs 14 days after injection of equal numbers of B16F10 cells with or without MLKL activation. Lower left: H&E staining of lung sections showing melanoma nodules. Right: quantification of lung metastatic nodules. $n = 5$ mice per group. Scale bar, 50 μm.

For *in vitro* assays, *n* represents individual channels or pores pooled from ≥3 independent experiments. For *in vivo* assays, *n* represents number of mice per group. Bars show mean ± SD; individual dots represent single measurement units (channel, pore, or mouse, depending on assay). Statistical analysis was performed using unpaired two-tailed Student's *t* test with Welch's correction. $^{*}p < 0.05$, $^{**}p < 0.01$, $^{****}p < 0.0001$; ns, not significant. All *p* values calculated from pooled data across all biological replicates; assays were repeated in ≥3 independent experiments with consistent outcomes.

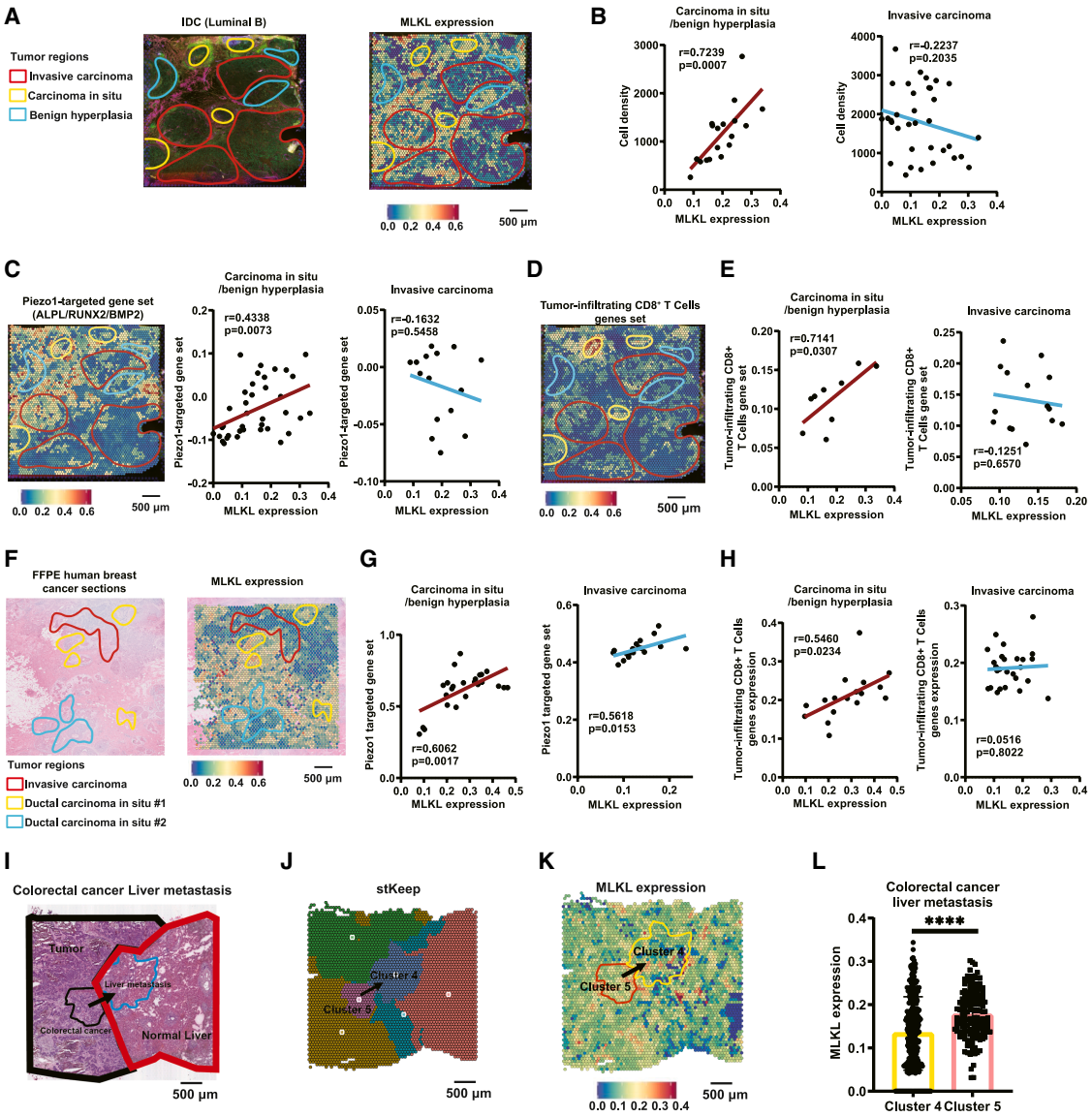


Figure 5. Tumor evolution selects for MLKL-low clones that escape necroptosis and anti-tumor immunity

(A) Spatial expression of MLKL correlates with malignancy grade in invasive ductal carcinoma (IDC) breast cancer (luminal B subtype). Left: representative immunofluorescent staining of IDC tissue sections from 13 regions showing invasive carcinoma (circled in red), carcinoma *in situ* (circled in orange), and benign hyperplasia (circled in blue). DAPI (blue), fiducial frame (green), and anti-CD3 (yellow) staining are indicated. Right: corresponding MLKL transcription levels in the same regions. MLKL expression is high in low-malignancy zones and low in high-malignancy zones.

(B) Pearson correlation analysis between cell density and spatial MLKL expression in carcinoma *in situ*/benign hyperplasia (less aggressive regions) (n = 18) versus invasive carcinoma (more aggressive regions) (n = 18).

(C) Spatial expression of PIEZO1 target genes (ALPL/RUNX2/BMP2) in the IDC breast cancer sample. Left: spatial gene expression map. Middle: Pearson correlation between MLKL and PIEZO1 target gene expression in carcinoma *in situ*/benign hyperplasia (less aggressive regions) (n = 37). Right: Pearson correlation in invasive carcinoma (more aggressive regions) (n = 15).

(D) Spatial expression of the tumor-infiltrating $CD8^+$ T cell-expressing gene set (TNF, IFNG, GZMB, and CD8A) in the IDC breast cancer sample.

(E) Pearson correlation analysis between MLKL expression and tumor-infiltrating $CD8^+$ T cell gene expression in carcinoma *in situ*/benign hyperplasia (left, less aggressive regions) (n = 9) versus invasive carcinoma (right, more aggressive regions) (n = 15).

(F) Spatial expression of MLKL correlates with malignancy grade in an formalin-fixed paraffin embedded (FFPE)-preserved breast cancer sample. Tissue sections from 8 regions showing invasive carcinoma (circled in red), ductal carcinoma *in situ* #1 (circled in orange), and ductal carcinoma *in situ* #2 (circled in blue) are presented.

(G) Spatial expression of PIEZO1 target genes (ALPL/RUNX2/BMP2) in the FFPE-preserved breast cancer sample. Left: spatial gene expression map. Middle: Pearson correlation between MLKL and PIEZO1 target gene expression in ductal carcinoma *in situ* #1/#2 (less aggressive regions) (n = 24). Right: Pearson correlation in invasive carcinoma (more aggressive regions) (n = 18).

(H) Pearson correlation analysis between MLKL expression and tumor-infiltrating $CD8^+$ T cell gene expression in ductal carcinoma *in situ* #1/#2 (left, less aggressive regions) (n = 17) versus invasive carcinoma (right, more aggressive regions) (n = 26) in the FFPE-preserved breast cancer sample.

(legend continued on next page)

Finally, we validated these findings *in vivo* using a B16F10 lung metastasis mouse model (Figure 4F). B16F10 cells with or without MLKL activation were injected into C57BL/6 mice, and lung metastasis was assessed 14 days post-injection. Consistent with our *in vitro* findings, the number of lung metastatic nodules was significantly reduced in mice injected with MLKL-activated cells compared with those injected with non-activated cells (Figure 4G).

Collectively, these results demonstrate that MLKL activation restricts cancer cell migration within physiologically confined microenvironments, thereby reducing metastatic dissemination.

Tumor evolution selects for MLKL-low clones that escape necroptosis and anti-tumor immunity

Having established MLKL's role in mechanosensing and cell death regulation in cancer cell lines, we next examined MLKL expression across malignancy stages in human tumor samples. Since high cell density creates mechanical compression that can promote MAT,[6,23,24,39–41] we reasoned that MAT-like conditions in solid tumors might modulate MLKL expression in a stage-dependent manner.

Early-stage tumors typically exhibit pronounced intratumoral heterogeneity,[20,42,43] providing adaptive flexibility under fluctuating microenvironmental constraints. As disease advances, clonal selection favors more aggressive populations with diminished heterogeneity, while progressive tumor expansion amplifies mechanical confinement. We hypothesized that escalating physical compression constitutes a selective pressure reshaping MLKL expression and clonal evolution during tumor progression.

To explore this, we leveraged spatially resolved transcriptomics (SRT) using a published breast cancer dataset from invasive ductal carcinoma (IDC) patients (luminal B subtype, 10× Genomics[44]), examining correlations between (1) MLKL levels and malignancy, (2) PIEZO1 activation and MLKL transcription, and (3) MLKL expression and immune infiltration.

We categorized tumor clusters by malignancy degree (Figures S6A and 5A, left). MLKL expression showed significant heterogeneity across clusters (Figure 5A, right), with relatively high expression in less aggressive clusters (benign hyperplasia, carcinoma *in situ*; green/orange) but low expression in invasive carcinoma (red).

MLKL expression positively correlated with cell density in less aggressive clusters but showed no correlation in invasive carcinoma (Figures 5B and S6B), suggesting MLKL is upregulated during early hyperproliferative stages (high cell density) but downregulated as aggressive, low-MLKL clones dominate in later stages.

We next examined correlations between MLKL and PIEZO1 target genes (ALPL/RUNX2/BMP2), given our earlier demonstration that PIEZO1 regulates MLKL transcription (Figure 2). PIEZO1 target genes were highly expressed and positively correlated with MLKL in less aggressive clusters, but significantly lower and uncorrelated with MLKL in invasive carcinoma (Figure 5C), indicating the PIEZO1-MLKL axis is active early but becomes uncoupled during progression toward invasive phenotypes.

Given that MLKL-mediated necroptosis promotes anti-tumor immunity through immunogenic cell death,[45–48] we investigated whether MLKL loss correlates with reduced immune infiltration. $CD8^+$ T cell gene expression was high in less aggressive regions (Figure 5D) and positively correlated with MLKL in carcinoma *in situ*/benign hyperplasia, but this correlation was lost in invasive carcinoma (Figure 5E), suggesting MLKL-low clones evade both necroptosis and anti-tumor immunity.

We validated these findings using an independent FFPE-preserved breast cancer sample[49] (Figure 5F). Consistent with the IDC sample, MLKL expression was high *in situ* (orange/green) but low in invasive regions (red). PIEZO1 target genes strongly correlated with MLKL in less aggressive regions but only moderately in invasive carcinoma (Figure 5G). PIEZO1 staining scores were markedly lower in invasive carcinoma (mostly <0.5) versus *in situ*/benign regions (mostly >0.5), mirroring MLKL's pattern (invasive: mostly <0.2; less aggressive: mostly >0.2). The MLKL-$CD8^+$ T cell correlation was similarly lost in invasive regions (Figure 5H), further supporting the MLKL-immune evasion link.

To confirm the spatial MLKL-STAT1 relationship, we analyzed both breast cancer samples: in aggressive invasive regions, MLKL and STAT1-targeted genes were concomitantly attenuated, while in less aggressive ductal carcinoma in situ (DCIS)/benign regions, they maintained strong positive correlation (Figures S6C and S6D)—providing *in situ* evidence for progressive loss of STAT1-driven MLKL regulation during tumor progression.

Extending to metastatic cancer, we analyzed SRT data from a colorectal cancer patient with liver metastasis (Figure 5I). Using stKeep spatial clustering[44] (Figure 5J), we identified primary tumor, liver metastasis, and normal liver regions. MLKL expression was significantly lower in metastatic regions versus primary tumor (Figures 5K and 5L), with correspondingly reduced $CD8^+$ T cell infiltration (Figure S6E), supporting that MLKL downregulation facilitates metastatic dissemination—consistent with our finding that MLKL activation limits cancer cell locomotion under confinement.

(I) H&E staining of colorectal cancer liver metastasis tissue with manual annotation of three regions: primary cancer (circled in black), liver metastasis (circled in blue), and normal liver tissue (circled in red).

(J) Spatial clustering analysis of colorectal cancer liver metastasis tissue using stLearn/stKeep. Detailed methodology is described in STAR Methods.

(K) Spatial expression of MLKL in colorectal cancer liver metastasis tissue based on stKeep spatial clustering analysis.

(L) Quantification of MLKL spatial expression across different regions in colorectal cancer liver metastasis tissue based on stKeep spatial clustering analysis (n = 324 in cluster 4; n = 146 in cluster 5).

Spatial transcriptomics and immunofluorescence performed on defined frozen or FFPE tissue sections as indicated; details provided in STAR Methods. All regional expression and correlation data are derived from independent ROIs within each sample; IDC dataset includes 13 ROIs, FFPE breast cancer sample includes 8 ROIs, and colorectal cancer liver metastasis sample includes 3 annotated regions. Scatterplots show individual ROIs; bars represent mean ± SD values across ROIs in each group.

Statistical analysis for group comparisons was performed using unpaired two-tailed Student's t test with Welch's correction. Correlation analyses were performed using Pearson correlation coefficient. ****$p < 0.0001$. All statistical tests used pooled data from all biological regions, not representative single runs.

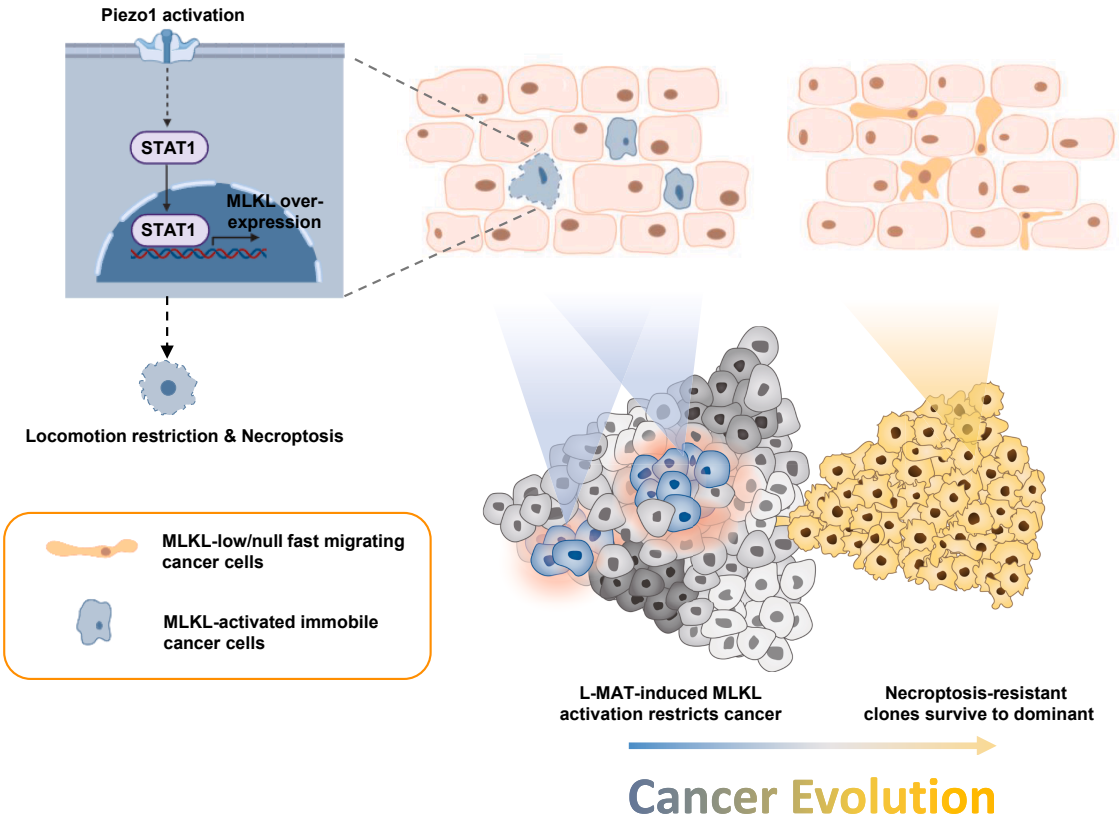


Figure 6. Model of L-MAT cancer cell necroptosis and migration restriction shaping tumor evolution

During cancer progression, sustained mechanical pressure to L-MAT cancer cells leads to MLKL overexpression, which restricts cell motility and ultimately triggers necroptosis. As tumors evolve, MLKL-low/null clones—resistant to necroptosis—become dominant. These clones retain strong migratory capacity with enhanced persistence, ultimately promoting rapid cancer progression and distant metastasis.

To evaluate RIPK3-independent MLKL regulation *in vivo*, we analyzed RIPK3 expression across these datasets. In both breast cancer samples, RIPK3 was consistently low throughout tumors, particularly in invasive zones, with no significant spatial correlation with MLKL in any region (Figures S7A and S7B). Similarly, in the colorectal cancer/liver metastasis dataset, RIPK3 remained low across both compartments with no significant RIPK3-MLKL correlation (Figure S7C). This consistent spatial decoupling across distinct tumor contexts provides *in vivo* evidence supporting RIPK3-independent MLKL regulation in human cancers.

Collectively, these data support a model in which MLKL upregulation serves a checkpoint-like role in tumor progression (Figure 6): promoting confinement-driven elimination of hyperproliferative cells via necroptosis while facilitating anti-tumor immunity and restricting metastatic dissemination by inhibiting MAT. Our spatial transcriptomic analyses reveal that reduced MLKL expression associates with advanced tumor stage and decreased immune infiltration, linking MLKL loss to immune evasion and metastatic progression. The convergence of experimental and transcriptomic evidence implicates intratumoral selection for MLKL-low cells as a mechanism enabling escape from necroptosis and immune surveillance, while licensing enhanced amoeboid migratory capacity to drive metastatic dissemination.

DISCUSSION

Rethinking necroptosis: A RIPK3-independent cell death modality

The canonical view of necroptosis positions RIPK3 as the obligate upstream activator of MLKL, typically triggered by death receptor ligation combined with caspase inhibitors. Our findings challenge this paradigm by demonstrating that MLKL-mediated necroptosis can occur independent of RIPK3 kinase activity, death receptor activation, or artificial compounds such as Smac mimetics and z-VAD. Mechanistically, the PIEZO1-STAT1 axis mediates transcriptional upregulation of MLKL, and the elevated MLKL accumulates on the membrane even without detectable RIPK3 expression. These findings suggest that necroptosis sensitivity *in vivo*—particularly within the 3D tumor microenvironment—may be substantially higher than previously appreciated from traditional 2D studies, revealing a physiologically relevant mode of necroptosis induction that warrants further structural and biochemical investigation.

The emerging concept of non-canonical necroptosis is further supported by the recent study of Kelepouras et al.,[50] which demonstrated that MLKL activation can occur independently of death-receptor signaling, yet still requires RIPK3 as an obligatory intermediate downstream of ZBP1, thereby retaining the core necrosome architecture. Our findings extend this

conceptual framework further, demonstrating that MLKL-driven cell death can occur in the complete absence of RIPK3. These two studies delineate at least two distinct layers of non-canonical necroptosis regulation, raising the intriguing possibility that additional, yet-to-be-discovered layers of MLKL regulation may exist —each bypassing distinct components of the canonical necrosome machinery under specific cellular or microenvironmental contexts.

MLKL as a tumor conditional checkpoint by governing L-MAT cell fate

MAT enables rapid, protease-independent migration that facilitates cancer cell dissemination. We introduce the concept of L-MAT—referring to cells with sustained MAT status under pressure—and demonstrate that MLKL activation determines L-MAT cell fate. MLKL-high cells undergoing L-MAT exhibit cellular paralysis characterized by an unpolarized, "fried egg" morphology, loss of actin retrograde flow, and eventual necroptotic cell death; in contrast, MLKL-low cells sustain L-MAT with enhanced migratory capacity, enabling successful dissemination. SRT support this model: MLKL expression is high and positively correlated with PIEZO1 activation in early-stage, less aggressive tumor regions, but markedly reduced and uncoupled from PIEZO1 signaling in invasive carcinoma and metastatic lesions. These observations establish MLKL as a *conditional checkpoint*—active in early tumor development but progressively inactivated through clonal selection of MLKL-low cells that bypass this checkpoint, escape necroptosis, evade anti-tumor immunity, and sustain productive amoeboid migration. This explains why aggressive clones exhibit reduced necroptosis sensitivity coupled with increased motility and suggests that MLKL could serve as a prognostic biomarker, with therapeutic strategies aimed at reinforcing this checkpoint in early-stage tumors or targeting compensatory pathways in advanced MLKL-low cancers.

PIEZO1 is a mechanically activated ion channel that rapidly responds to membrane tension but undergoes inactivation and adaptive gating during repetitive or sustained mechanical stimulation, thereby limiting prolonged mechanotransduction.[51,52] Building on this established framework, we propose that cancer cells experience persistent cycles of mechanical confinement while repeatedly traversing dense ECMs and narrow tissue spaces. Such recurrent mechanical stimulation would be expected to progressively attenuate PIEZO1 responsiveness over extended time scales, reducing PIEZO1-dependent MLKL signaling and allowing cells to evade this intrinsic necroptotic checkpoint. Consistent with this model, our findings identify MLKL as a confinement-induced barrier to amoeboid dissemination and support a model in which mechanical adaptation promotes the selection of necroptosis-resistant, more invasive tumor clones. Additional mechanisms may contribute to MLKL loss *in vivo*, including clonal mutations at the MLKL locus, alterations in RIPK3 status, or broader rewiring of mechanotransduction networks disrupting the PIEZO1-STAT1-MLKL axis; distinguishing among these will require future functional studies in physiologically relevant tumor models.

Our findings suggest that mechanically induced cell death checkpoints are dynamic barriers whose progressive evasion represents a fundamental mechanism by which cancer cells acquire metastatic fitness. Whether attenuation of mechanosensitive signaling during chronic confinement occurs through intrinsic remodeling of PIEZO1 activity or broader rewiring of mechanotransduction networks remains an important open question. Therapeutic strategies that restore or reinforce these intrinsic mechanosensitive checkpoints may therefore provide an avenue for limiting tumor progression and metastatic dissemination.

Local immune modulation by MLKL activation

A notable feature of MLKL activation during L-MAT is that arrested cells are immobilized long before they ultimately undergo necroptosis, meaning that cellular contents released upon membrane rupture—including immunogenic damage-associated molecular patterns (DAMPs)—are deposited locally rather than disseminated to distant tissues. This spatially restricted release raises the possibility that L-MAT-induced necroptosis may actively recruit and activate immune effectors within the tumor microenvironment. Consistent with this idea, our analyses reveal a positive correlation between MLKL expression and tumor-infiltrating $CD8^+$ T cells in less aggressive tumor regions, a correlation lost in invasive carcinoma. These findings suggest that MLKL-mediated cell death during L-MAT provides a dual mechanism of tumor suppression—direct elimination of malignant cells and enhanced local immune surveillance—that could be harnessed for early-stage cancer immunotherapy.

Although MLKL has been extensively studied as the terminal executioner of necroptosis, its potential impact on cell behavior before plasma membrane rupture has received far less attention. In conventional 2D models, rapid membrane permeabilization following MLKL activation makes it difficult to distinguish direct effects of MLKL from terminal membrane disruption. Nevertheless, accumulating evidence indicates that MLKL activation is accompanied by early cellular events preceding rupture, including cell rounding, blebbing, loss of adhesion, and membrane remodeling,[34,53–55] all closely linked to cortical actomyosin dynamics. In our L-MAT model, prolonged confinement uncouples these early events from overt membrane rupture, revealing that MLKL activation progressively restricts fast amoeboid migration well before detectable plasma membrane damage. This argues that impaired locomotion reflects an earlier function of activated MLKL in disrupting the migratory machinery, rather than a secondary consequence of membrane permeabilization—an effect likely pronounced under confinement, where amoeboid migration critically depends on sustained cortical actomyosin remodeling and front-rear polarity. By temporally separating locomotion defects from terminal membrane rupture, the L-MAT model provides an experimental platform to dissect the direct consequences of MLKL activation on the migratory machinery, uncovering a previously unappreciated functional connection between MLKL and restriction of amoeboid migration that extends its role beyond a membrane-lytic effector. Defining the molecular mechanisms by which activated MLKL remodels the cortical cytoskeleton and migratory apparatus will be an important direction for future investigation.

PIEZO1 activation extends to diverse mechanically challenged cell types

PIEZO1 activation is not restricted to mesenchymal cells. Professional amoeboid cells—including neutrophils, T and B lymphocytes, dendritic cells, and macrophages—intrinsically migrate in

an amoeboid mode and frequently encounter mechanical confinement *in vivo*. PIEZO1 is activated in several of these cell types under physiologically relevant confinement or deformation: *trans*-endothelial migration induces membrane tension–dependent PIEZO1 activation and Ca^{2+} influx in neutrophils,[56,57] pulmonary capillary confinement activates PIEZO1 to regulate neutrophil functional specialization,[58] PIEZO1 modulates T cell receptor signaling,[59,60] dendritic cell mechanosensing regulates cytokine production and T cell differentiation,[33] and macrophages respond to substrate stiffness and mechanical confinement.[32,61]

Whether PIEZO1 activation in these professional amoeboid cells also induces MLKL-dependent necroptosis under specific physiological or pathological contexts remains unknown and warrants systematic investigation using appropriate *in vivo* and *in vitro* models. Our study provides a conceptual framework for exploring this possibility in future work.

Other forms of cell death contribute to L-MAT cell fate

In our experimental setting, we excluded the involvement of reactive oxygen species (ROS) and apoptosis in L-MAT-induced cell death. The lack of ROS involvement also rules out ferroptosis, which is fundamentally dependent on lipid peroxidation driven by reactive oxygen species. However, we observed that additional MLKL-independent death modalities may contribute to cell fate under these conditions. The identity of these alternative pathways remains unclear and warrants further investigation. Given the substantial membrane, nuclear, and cytoskeletal stress imposed by prolonged confinement in non-adhesive environments, additional death mechanisms may operate in parallel with or independently of necroptosis. Unbiased approaches such as CRISPR screens or phosphoproteomics may help identify MLKL-independent contributors to L-MAT-induced cell death.

Limitations of the study

While our study establishes MLKL as a conditional checkpoint governing L-MAT cell fate and identifies the PIEZO1-STAT1-MLKL axis as a driver of confinement-induced necroptosis, several important limitations remain. First, although our work provides a tractable assay system for dissecting the crosstalk between MLKL activation and actin cortex dynamics in the L-MAT scenario, the precise molecular mechanism by which MLKL activation leads to migration restriction prior to membrane rupture—in particular, how membrane-associated MLKL disturbs the actin cortex to impair amoeboid motility—remains incompletely understood. Second, our patient tumor data suggest that persistent cycles of mechanical confinement during cancer evolution progressively desensitize PIEZO1 responsiveness over extended timescales *in vivo*; however, how such prolonged desensitization ultimately silences MLKL transcription at the molecular level has not been resolved. Third, while our spatial transcriptomic analyses of patient tumors reveal a strong correlation between MLKL expression, PIEZO1 activation, and clonal aggressiveness, functional validation of the PIEZO1-STAT1-MLKL axis as a therapeutic vulnerability *in vivo*, particularly in preclinical metastasis models, is currently lacking. Together, these limitations underscore the need for further mechanistic and translational investigation into confinement-induced necroptosis as an evolutionary bottleneck in cancer progression.

RESOURCE AVAILABILITY

Lead contact

Requests for further information and resources should be directed to and will be fulfilled by the lead contact, Dr. Liming Sun (liming.sun@sibcb.ac.cn).

Materials availability

All unique/stable reagents generated in this study are available from the lead contact with a completed materials transfer agreement.

Data and code availability

Raw sequencing data have been deposited at GEO as GEO: GSE328527 and GSE328536 and are publicly available as of the date of publication. This paper does not report original code. Any additional information required to reanalyze the data reported in this paper is available from the lead contact upon request.

ACKNOWLEDGMENTS

We thank members of the Sun laboratory for their comments and suggestions. We thank Drs. Mohamed Lamkanfi, Lieselotte Vande Walle, and Henning Walczak for their valuable suggestions on the revised manuscript. We thank the Chemical & Molecular Biology Facility and the Cell Biology Facility of SIBCB for their assistance with inhibitor screening. This work was supported by the National Key Research and Development Program of China (2023YFA0914903), CAS Youth Interdisciplinary Team, the National Natural Science Foundation of China (22274026 and 32570769), Tianfu Jincheng Laboratory (TFJCPI20260001), and the Innovative Research Team of High-Level Local Universities in Shanghai (SHSMU-ZDCX20212000).

AUTHOR CONTRIBUTIONS

L.S. and Y.-J.L. conceived the project; W.Z. designed and performed the majority of experiments; Y.-J.W. performed the cell confinement and vascular chip experiments; C.Z., G.W., and X.M. did the bioinformatics analysis; J.H. and N.Y. helped with the animal experiments; B.-Q. L. helped cell confinement experiments and cell collection; the other authors offered technical support; L.S., Y.-J.L., W.Z., Y.-J.W., and C.Z. wrote the manuscript; and all authors discussed the results and commented on the manuscript.

DECLARATION OF INTERESTS

The authors declare no competing interests.

STAR★METHODS

Detailed methods are provided in the online version of this paper and include the following:

- KEY RESOURCES TABLE
- EXPERIMENTAL MODEL AND STUDY PARTICIPANT DETAILS
  - Animals
  - Cell Lines
- METHOD DETAILS
  - Reagents
  - SYTOX Green/PI Staining Assay
  - ATP Assay
  - Acquisition of MLKL-Activated Survivor Cells
  - Immunohistochemistry Staining
  - Immunofluorescence staining
  - Fabrication of the Cell Confiner
  - Live Cell Imaging
  - Image Analysis
  - Transcriptomic analysis of HeLa cells under L-MAT
  - Gene Ontology Enrichment Analysis
  - Transwell Assay
  - Microfluidic Chip Assay
  - SRT Dataset and Bioinformatics Analyses
- QUANTIFICATION AND STATISTICAL ANALYSIS

SUPPLEMENTAL INFORMATION

Supplemental information can be found online at https://doi.org/10.1016/j.devcel.2026.09.003.

Received: April 7, 2026
Revised: July 2, 2026
Accepted: September 10, 2026
Published: October 14, 2026

REFERENCES

1. Graziani, V., Rodriguez-Hernandez, I., Maiques, O., and Sanz-Moreno, V. (2022). The amoeboid state as part of the epithelial-to-mesenchymal transition programme. Trends Cell Biol. *32*, 228–242. https://doi.org/10.1016/j.tcb.2021.10.004.
2. Friedl, P., and Wolf, K. (2003). Tumour-cell invasion and migration: diversity and escape mechanisms. Nat. Rev. Cancer *3*, 362–374. https://doi.org/10.1038/nrc1075.
3. Lämmermann, T., Bader, B.L., Monkley, S.J., Worbs, T., Wedlich-Söldner, R., Hirsch, K., Keller, M., Förster, R., Critchley, D.R., Fässler, R., and Sixt, M. (2008). Rapid leukocyte migration by integrin-independent flowing and squeezing. Nature *453*, 51–55. https://doi.org/10.1038/nature06887.
4. Panková, K., Rösel, D., Novotný, M., and Brábek, J. (2010). The molecular mechanisms of transition between mesenchymal and amoeboid invasiveness in tumor cells. Cell. Mol. Life Sci. *67*, 63–71. https://doi.org/10.1007/s00018-009-0132-1.
5. Tozluoğlu, M., Tournier, A.L., Jenkins, R.P., Hooper, S., Bates, P.A., and Sahai, E. (2013). Matrix geometry determines optimal cancer cell migration strategy and modulates response to interventions. Nat. Cell Biol. *15*, 751–762. https://doi.org/10.1038/ncb2775.
6. Liu, Y.J., Le Berre, M., Lautenschlaeger, F., Maiuri, P., Callan-Jones, A., Heuzé, M., Takaki, T., Voituriez, R., and Piel, M. (2015). Confinement and low adhesion induce fast amoeboid migration of slow mesenchymal cells. Cell *160*, 659–672. https://doi.org/10.1016/j.cell.2015.01.007.
7. Sun, L., Wang, H., Wang, Z., He, S., Chen, S., Liao, D., Wang, L., Yan, J., Liu, W., Lei, X., and Wang, X. (2012). Mixed lineage kinase domain-like protein mediates necrosis signaling downstream of RIP3 kinase. Cell *148*, 213–227. https://doi.org/10.1016/j.cell.2011.11.031.
8. Wang, H., Sun, L., Su, L., Rizo, J., Liu, L., Wang, L.F., Wang, F.S., and Wang, X. (2014). Mixed lineage kinase domain-like protein MLKL causes necrotic membrane disruption upon phosphorylation by RIP3. Mol. Cell *54*, 133–146. https://doi.org/10.1016/j.molcel.2014.03.003.
9. Hildebrand, J.M., Tanzer, M.C., Lucet, I.S., Young, S.N., Spall, S.K., Sharma, P., Pierotti, C., Garnier, J.M., Dobson, R.C.J., Webb, A.I., et al. (2014). Activation of the pseudokinase MLKL unleashes the four-helix bundle domain to induce membrane localization and necroptotic cell death. Proc. Natl. Acad. Sci. USA *111*, 15072–15077. https://doi.org/10.1073/pnas.1408987111.
10. Dondelinger, Y., Declercq, W., Montessuit, S., Roelandt, R., Goncalves, A., Bruggeman, I., Hulpiau, P., Weber, K., Sehon, C.A., Marquis, R.W., et al. (2014). MLKL compromises plasma membrane integrity by binding to phosphatidylinositol phosphates. Cell Rep. *7*, 971–981. https://doi.org/10.1016/j.celrep.2014.04.026.
11. Cai, Z., Jitkaew, S., Zhao, J., Chiang, H.C., Choksi, S., Liu, J., Ward, Y., Wu, L.G., and Liu, Z.G. (2014). Plasma membrane translocation of trimerized MLKL protein is required for TNF-induced necroptosis. Nat. Cell Biol. *16*, 55–65. https://doi.org/10.1038/ncb2883.
12. Chen, X., Li, W., Ren, J., Huang, D., He, W.T., Song, Y., Yang, C., Li, W., Zheng, X., Chen, P., and Han, J. (2014). Translocation of mixed lineage kinase domain-like protein to plasma membrane leads to necrotic cell death. Cell Res. *24*, 105–121. https://doi.org/10.1038/cr.2013.171.
13. Murphy, J.M., Czabotar, P.E., Hildebrand, J.M., Lucet, I.S., Zhang, J.G., Alvarez-Diaz, S., Lewis, R., Lalaoui, N., Metcalf, D., Webb, A.I., et al. (2013). The pseudokinase MLKL mediates necroptosis via a molecular switch mechanism. Immunity *39*, 443–453. https://doi.org/10.1016/j.immuni.2013.06.018.
14. He, S., Wang, L., Miao, L., Wang, T., Du, F., Zhao, L., and Wang, X. (2009). Receptor interacting protein kinase-3 determines cellular necrotic response to TNF-alpha. Cell *137*, 1100–1111. https://doi.org/10.1016/j.cell.2009.05.021.
15. Folkman, J., and Hochberg, M. (1973). Self-regulation of growth in three dimensions. J. Exp. Med. *138*, 745–753. https://doi.org/10.1084/jem.138.4.745.
16. Rahimi Koshkaki, H., Minasi, S., Ugolini, A., Trevisi, G., Napoletano, C., Zizzari, I.G., Gessi, M., Giangaspero, F., Mangiola, A., Nuti, M., et al. (2020). Immunohistochemical Characterization of Immune Infiltrate in Tumor Microenvironment of Glioblastoma. J. Pers. Med. *10*, 112. https://doi.org/10.3390/jpm10030112.
17. Suzuki, J., Kojima, M., Aokage, K., Sakai, T., Nakamura, H., Ohara, Y., Tane, K., Miyoshi, T., Sugano, M., Fujii, S., et al. (2019). Clinicopathological characteristics associated with necrosis in pulmonary metastases from colorectal cancer. Virchows Arch. *474*, 569–575. https://doi.org/10.1007/s00428-019-02535-7.
18. Gong, Y., Fan, Z., Luo, G., Yang, C., Huang, Q., Fan, K., Cheng, H., Jin, K., Ni, Q., Yu, X., and Liu, C. (2019). The role of necroptosis in cancer biology and therapy. Mol. Cancer *18*, 100. https://doi.org/10.1186/s12943-019-1029-8.
19. Greaves, M., and Maley, C.C. (2012). Clonal evolution in cancer. Nature *481*, 306–313. https://doi.org/10.1038/nature10762.
20. McGranahan, N., and Swanton, C. (2017). Clonal Heterogeneity and Tumor Evolution: Past, Present, and the Future. Cell *168*, 613–628. https://doi.org/10.1016/j.cell.2017.01.018.
21. Massey, A., Stewart, J., Smith, C., Parvini, C., McCormick, M., Do, K., and Cartagena-Rivera, A.X. (2024). Mechanical properties of human tumour tissues and their implications for cancer development. Nat. Rev. Phys. *6*, 269–282. https://doi.org/10.1038/s42254-024-00707-2.
22. Stylianopoulos, T., Martin, J.D., Snuderl, M., Mpekris, F., Jain, S.R., and Jain, R.K. (2013). Coevolution of solid stress and interstitial fluid pressure in tumors during progression: implications for vascular collapse. Cancer Res. *73*, 3833–3841. https://doi.org/10.1158/0008-5472.CAN-12-4521.
23. Bergert, M., Erzberger, A., Desai, R.A., Aspalter, I.M., Oates, A.C., Charras, G., Salbreux, G., and Paluch, E.K. (2015). Force transmission during adhesion-independent migration. Nat. Cell Biol. *17*, 524–529. https://doi.org/10.1038/ncb3134.
24. Ruprecht, V., Wieser, S., Callan-Jones, A., Smutny, M., Morita, H., Sako, K., Barone, V., Ritsch-Marte, M., Sixt, M., Voituriez, R., and Heisenberg, C.P. (2015). Cortical contractility triggers a stochastic switch to fast amoeboid cell motility. Cell *160*, 673–685. https://doi.org/10.1016/j.cell.2015.01.008.
25. Hung, W.C., Yang, J.R., Yankaskas, C.L., Wong, B.S., Wu, P.H., Pardo-Pastor, C., Serra, S.A., Chiang, M.J., Gu, Z., Wirtz, D., et al. (2016). Confinement Sensing and Signal Optimization via Piezo1/PKA and Myosin II Pathways. Cell Rep. *15*, 1430–1441. https://doi.org/10.1016/j.celrep.2016.04.035.
26. Srivastava, N., Traynor, D., Piel, M., Kabla, A.J., and Kay, R.R. (2020). Pressure sensing through Piezo channels controls whether cells migrate with blebs or pseudopods. Proc. Natl. Acad. Sci. USA *117*, 2506–2512. https://doi.org/10.1073/pnas.1905730117.
27. Kar, N., Caruso, A.P., Prokopiou, N., Abrenica, A., and Logue, J.S. (2025). The activation of INF2 by Piezo1/Ca2+ is required for mesenchymal-to-amoeboid transition in confined environments. Curr. Biol. *35*, 1791–1804.e5. https://doi.org/10.1016/j.cub.2025.02.066.
28. Bae, C., Sachs, F., and Gottlieb, P.A. (2011). The mechanosensitive ion channel Piezo1 is inhibited by the peptide GsMTx4. Biochemistry *50*, 6295–6300. https://doi.org/10.1021/bi200770q.
29. Yang, A., Zhang, J., Huang, T., Yu, Z., Zhao, C., Xu, Y., and Ma, B. (2023). Role of CREB1 dysregulation in calcium oxalate monohydrate

crystals-induced tubular epithelial cell injury. Mol. Cell. Toxicol. *20*, 939–948. https://doi.org/10.1007/s13273-023-00404-8.

30. Syeda, R., Xu, J., Dubin, A.E., Coste, B., Mathur, J., Huynh, T., Matzen, J., Lao, J., Tully, D.C., Engels, I.H., et al. (2015). Chemical activation of the mechanotransduction channel Piezo1. eLife *4*, e07369. https://doi.org/10.7554/eLife.07369.
31. Coste, B., Mathur, J., Schmidt, M., Earley, T.J., Ranade, S., Petrus, M.J., Dubin, A.E., and Patapoutian, A. (2010). Piezo1 and Piezo2 are essential components of distinct mechanically activated cation channels. Science *330*, 55–60. https://doi.org/10.1126/science.1193270.
32. Atcha, H., Jairaman, A., Holt, J.R., Meli, V.S., Nagalla, R.R., Veerasubramanian, P.K., Brumm, K.T., Lim, H.E., Othy, S., Cahalan, M.D., et al. (2021). Mechanically activated ion channel Piezo1 modulates macrophage polarization and stiffness sensing. Nat. Commun. *12*, 3256. https://doi.org/10.1038/s41467-021-23482-5.
33. Wang, Y., Yang, H., Jia, A., Wang, Y., Yang, Q., Dong, Y., Hou, Y., Cao, Y., Dong, L., Bi, Y., et al. (2022). Dendritic cell Piezo1 directs the differentiation of TH1 and Treg cells in cancer. eLife *11*, e79957. https://doi.org/10.7554/eLife.79957.
34. Gong, Y.N., Guy, C., Olauson, H., Becker, J.U., Yang, M., Fitzgerald, P., Linkermann, A., and Green, D.R. (2017). ESCRT-III Acts Downstream of MLKL to Regulate Necroptotic Cell Death and Its Consequences. Cell *169*, 286–300.e16. https://doi.org/10.1016/j.cell.2017.03.020.
35. Paluch, E.K., Aspalter, I.M., and Sixt, M. (2016). Focal Adhesion-Independent Cell Migration. Annu. Rev. Cell Dev. Biol. *32*, 469–490. https://doi.org/10.1146/annurev-cellbio-111315-125341.
36. Bremer, C., Tung, C.H., and Weissleder, R. (2001). In vivo molecular target assessment of matrix metalloproteinase inhibition. Nat. Med. *7*, 743–748. https://doi.org/10.1038/89126.
37. Fisher, K.E., Sacharidou, A., Stratman, A.N., Mayo, A.M., Fisher, S.B., Mahan, R.D., Davis, M.J., and Davis, G.E. (2009). MT1-MMP- and Cdc42-dependent signaling co-regulate cell invasion and tunnel formation in 3D collagen matrices. J. Cell Sci. *122*, 4558–4569. https://doi.org/10.1242/jcs.050724.
38. Jiang, K., Liang, L., and Lim, C.T. (2021). Engineering confining microenvironment for studying cancer metastasis. iScience *24*, 102098. https://doi.org/10.1016/j.isci.2021.102098.
39. Doolin, M.T., Smith, I.M., and Stroka, K.M. (2021). Fibroblast to myofibroblast transition is enhanced by increased cell density. Mol. Biol. Cell *32*, ar41. https://doi.org/10.1091/mbc.E20-08-0536.
40. Wolf, K., Te Lindert, M., Krause, M., Alexander, S., Te Riet, J., Willis, A.L., Hoffman, R.M., Figdor, C.G., Weiss, S.J., and Friedl, P. (2013). Physical limits of cell migration: control by ECM space and nuclear deformation and tuning by proteolysis and traction force. J. Cell Biol. *201*, 1069–1084. https://doi.org/10.1083/jcb.201210152.
41. Petrie, R.J., and Yamada, K.M. (2016). Multiple mechanisms of 3D migration: the origins of plasticity. Curr. Opin. Cell Biol. *42*, 7–12. https://doi.org/10.1016/j.ceb.2016.03.025.
42. Dagogo-Jack, I., and Shaw, A.T. (2018). Tumour heterogeneity and resistance to cancer therapies. Nat. Rev. Clin. Oncol. *15*, 81–94. https://doi.org/10.1038/nrclinonc.2017.166.
43. Meacham, C.E., and Morrison, S.J. (2013). Tumour heterogeneity and cancer cell plasticity. Nature *501*, 328–337. https://doi.org/10.1038/nature12624.
44. Zuo, C., Xia, J., and Chen, L. (2024). Dissecting tumor microenvironment from spatially resolved transcriptomics data by heterogeneous graph learning. Nat. Commun. *15*, 5057. https://doi.org/10.1038/s41467-024-49171-7.
45. Kroemer, G., Galluzzi, L., Kepp, O., and Zitvogel, L. (2013). Immunogenic cell death in cancer therapy. Annu. Rev. Immunol. *31*, 51–72. https://doi.org/10.1146/annurev-immunol-032712-100008.
46. Aaes, T.L., Kaczmarek, A., Delvaeye, T., De Craene, B., De Koker, S., Heyndrickx, L., Delrue, I., Taminau, J., Wiernicki, B., De Groote, P., et al. (2016). Vaccination with Necroptotic Cancer Cells Induces Efficient Anti-tumor Immunity. Cell Rep. *15*, 274–287. https://doi.org/10.1016/j.celrep.2016.03.037.
47. Snyder, A.G., Hubbard, N.W., Messmer, M.N., Kofman, S.B., Hagan, C.E., Orozco, S.L., Chiang, K., Daniels, B.P., Baker, D., and Oberst, A. (2019). Intratumoral activation of the necroptotic pathway components RIPK1 and RIPK3 potentiates antitumor immunity. Sci. Immunol. *4*, eaaw2004. https://doi.org/10.1126/sciimmunol.aaw2004.
48. Yatim, N., Jusforgues-Saklani, H., Orozco, S., Schulz, O., Barreira da Silva, R., Reis e Sousa, C., Green, D.R., Oberst, A., and Albert, M.L. (2015). RIPK1 and NF-kappaB signaling in dying cells determines cross-priming of CD8(+) T cells. Science *350*, 328–334. https://doi.org/10.1126/science.aad0395.
49. Janesick, A., Shelansky, R., Gottscho, A.D., Wagner, F., Williams, S.R., Rouault, M., Beliakoff, G., Morrison, C.A., Oliveira, M.F., Sicherman, J.T., et al. (2023). High resolution mapping of the tumor microenvironment using integrated single-cell, spatial and in situ analysis. Nat. Commun. *14*, 8353. https://doi.org/10.1038/s41467-023-43458-x.
50. Kelepouras, K., Saggau, J., Bonasera, D., Kiefer, C., Locci, F., Rakhsh-Khorshid, H., Grauvogel, L., Varanda, A.B., Peifer, M., Loricchio, E., et al. (2025). STING induces ZBP1-mediated necroptosis independently of TNFR1 and FADD. Nature *647*, 735–746. https://doi.org/10.1038/s41586-025-09536-4.
51. Zhou, Z., and Martinac, B. (2023). Mechanisms of PIEZO Channel Inactivation. Int. J. Mol. Sci. *24*, 14113. https://doi.org/10.3390/ijms241814113.
52. Lewis, A.H., Cui, A.F., McDonald, M.F., and Grandl, J. (2017). Transduction of Repetitive Mechanical Stimuli by Piezo1 and Piezo2 Ion Channels. Cell Rep. *19*, 2572–2585. https://doi.org/10.1016/j.celrep.2017.05.079.
53. de Vasconcelos, N.M., Van Opdenbosch, N., Van Gorp, H., Parthoens, E., and Lamkanfi, M. (2019). Single-cell analysis of pyroptosis dynamics reveals conserved GSDMD-mediated subcellular events that precede plasma membrane rupture. Cell Death Differ. *26*, 146–161. https://doi.org/10.1038/s41418-018-0106-7.
54. Hu, X.M., Li, Z.X., Lin, R.H., Shan, J.Q., Yu, Q.W., Wang, R.X., Liao, L.S., Yan, W.T., Wang, Z., Shang, L., et al. (2021). Guidelines for Regulated Cell Death Assays: A Systematic Summary, A Categorical Comparison, A Prospective. Front. Cell Dev. Biol. *9*, 634690. https://doi.org/10.3389/fcell.2021.634690.
55. Yoon, S., Kovalenko, A., Bogdanov, K., and Wallach, D. (2017). MLKL, the Protein that Mediates Necroptosis, Also Regulates Endosomal Trafficking and Extracellular Vesicle Generation. Immunity *47*, 51–65.e7. https://doi.org/10.1016/j.immuni.2017.06.001.
56. Zhao, W., Wang, J., and Wang, J. (2025). Mechanotransduction in neutrophil: Mechanosensing and immune function regulation. Mechanobiol. Med. *3*, 100157. https://doi.org/10.1016/j.mbm.2025.100157.
57. Mukhopadhyay, A., Tsukasaki, Y., Chan, W.C., Le, J.P., Kwok, M.L., Zhou, J., Natarajan, V., Mostafazadeh, N., Maienschein-Cline, M., Papautsky, I., et al. (2024). trans-Endothelial neutrophil migration activates bactericidal function via Piezo1 mechanosensing. Immunity *57*, 52–67.e10. https://doi.org/10.1016/j.immuni.2023.11.007.
58. Wang, J., Zhao, W., Bai, W., Dong, D., Wang, H., Qi, X., Thanabalasuriar, A., Ye, Y., Xu, T.L., Li, H., et al. (2025). PIEZO1 mediates mechanical reprogramming of neutrophils for proangiogenic specialization in the lung. J. Clin. Investig. *135*, e183796. https://doi.org/10.1172/JCI183796.
59. Liu, C.S.C., Raychaudhuri, D., Paul, B., Chakrabarty, Y., Ghosh, A.R., Rahaman, O., Talukdar, A., and Ganguly, D. (2018). Cutting Edge: Piezo1 Mechanosensors Optimize Human T Cell Activation. J. Immunol. *200*, 1255–1260. https://doi.org/10.4049/jimmunol.1701118.
60. Hope, J.M., Dombroski, J.A., Pereles, R.S., Lopez-Cavestany, M., Greenlee, J.D., Schwager, S.C., Reinhart-King, C.A., and King, M.R. (2022). Fluid shear stress enhances T cell activation through Piezo1. BMC Biol. *20*, 61. https://doi.org/10.1186/s12915-022-01266-7.
61. Solis, A.G., Bielecki, P., Steach, H.R., Sharma, L., Harman, C.C.D., Yun, S., de Zoete, M.R., Warnock, J.N., To, S.D.F., York, A.G., et al. (2019).

Mechanosensation of cyclical force by PIEZO1 is essential for innate immunity. Nature *573*, 69–74. https://doi.org/10.1038/s41586-019-1485-8.

62. Schindelin, J., Arganda-Carreras, I., Frise, E., Kaynig, V., Longair, M., Pietzsch, T., Preibisch, S., Rueden, C., Saalfeld, S., Schmid, B., et al. (2012). Fiji: an open-source platform for biological-image analysis. Nat. Methods *9*, 676–682. https://doi.org/10.1038/nmeth.2019.
63. Love, M.I., Huber, W., and Anders, S. (2014). Moderated estimation of fold change and dispersion for RNA-seq data with DESeq2. Genome Biol. *15*, 550. https://doi.org/10.1186/s13059-014-0550-8.
64. Liao, Y., Smyth, G.K., and Shi, W. (2014). featureCounts: an efficient general purpose program for assigning sequence reads to genomic features. Bioinformatics *30*, 923–930. https://doi.org/10.1093/bioinformatics/btt656.
65. Kim, D., Paggi, J.M., Park, C., Bennett, C., and Salzberg, S.L. (2019). Graph-based genome alignment and genotyping with HISAT2 and HISAT-genotype. Nat. Biotechnol. *37*, 907–915. https://doi.org/10.1038/s41587-019-0201-4.
66. Le Berre, M., Aubertin, J., and Piel, M. (2012). Fine control of nuclear confinement identifies a threshold deformation leading to lamina rupture and induction of specific genes. Integr. Biol. (Camb.) *4*, 1406–1414. https://doi.org/10.1039/c2ib20056b.
67. Xia, Y., and Whitesides, G.M. (1998). Soft Lithography. Angew. Chem. Int. Ed. *37*, 550–575. https://doi.org/10.1002/(SICI)1521-3773(19980316)37:5<550::AID-ANIE550>3.0.CO;2-G.
68. Thiam, H.R., Vargas, P., Carpi, N., Crespo, C.L., Raab, M., Terriac, E., King, M.C., Jacobelli, J., Alberts, A.S., Stradal, T., et al. (2016). Perinuclear Arp2/3-driven actin polymerization enables nuclear deformation to facilitate cell migration through complex environments. Nat. Commun. *7*, 10997. https://doi.org/10.1038/ncomms10997.
69. Heuzé, M.L., Collin, O., Terriac, E., Lennon-Duménil, A.M., and Piel, M. (2011). Cell migration in confinement: a micro-channel-based assay. Methods Mol. Biol. *769*, 415–434. https://doi.org/10.1007/978-1-61779-207-6_28.
70. Russell, B.C., Torralba, A., Murphy, K.P., and Freeman, W.T. (2008). LabelMe: a database and web-based tool for image annotation. Int. J. Comput. Vis. *77*, 157–173. https://doi.org/10.1007/s11263-007-0090-8.
71. Hartman, S.E., Bertone, P., Nath, A.K., Royce, T.E., Gerstein, M., Weissman, S., and Snyder, M. (2005). Global changes in STAT target selection and transcription regulation upon interferon treatments. Genes Dev. *19*, 2953–2968. https://doi.org/10.1101/gad.1371305.
72. Tirosh, I., Izar, B., Prakadan, S.M., Wadsworth, M.H., Treacy, D., Trombetta, J.J., Rotem, A., Rodman, C., Lian, C., Murphy, G., et al. (2016). Dissecting the multicellular ecosystem of metastatic melanoma by single-cell RNA-seq. Science *352*, 189–196. https://doi.org/10.1126/science.aad0501.

STAR★METHODS

KEY RESOURCES TABLE

REAGENT or RESOURCE	SOURCE	IDENTIFIER
Antibodies		
Rabbit polyclonal anti-M Mlkl	Abgent	cat#AP14272b; RRID: AB_11134649
Rabbit monoclonal anti-phospho-MLKL (S358)	Abcam	cat#ab187091; Clone EPR9514; RRID: AB_2619685
Rabbit Monoclonal anti-MLKL (D2I6N)	Cell Signaling Technology	cat#14993; RRID: AB_2721822
Rabbit polyclonal anti-STAT1	Cell Signaling Technology	cat#9172; RRID: AB_2198300
Mouse monoclonal anti-FAM38A / PIEZO1	HUABIO	cat#M1005-2; RRID: AB_3073014
Mouse Monoclonal anti-Flag M2-peroxidase (HRP)	Sigma-Aldrich	cat#A8592; RRID: AB_439702
Rabbit Polyclonal anti-RIP3	Abcam	cat#ab226297; RRID: N/A
Mouse Monoclonal anti-β-Actin	ABclonal	cat#AC004; RRID: AB_2737399
Rabbit polyclonal anti-COX IV	Proteintech	cat#11242-1-AP; RRID: AB_2085278
Mouse Monoclonal anti-GAPDH	ABclonal	cat#AC033; RRID: AB_2769570
Rabbit Polyclonal anti-Phospho-STAT1 (Tyr701) (58D6)	Cell Signaling Technology	cat#9167; RRID: AB_561284
Bacterial and virus strains		
DH5α Chemically Competent Cell	Tsingke	cat#TSC-C14
Chemicals, peptides, and recombinant proteins		
Recombinant TNF	This paper	N/A
Smac mimetic	This paper	N/A
z-VAD-FMK	This paper	N/A
GsMTx4	MedChemExpress	HY-P1410; CAS: 1209500-46-8
Tacrolimus (FK506)	MedChemExpress	HY-13756; CAS: 104987-11-3
N-Acetylcysteine	MedChemExpress	HY-B0215; CAS: 616-91-1
BAPTA-AM	MedChemExpress	HY-100545; CAS: 126150-97-8
B/B Homodimerizer (AP20187)	MedChemExpress	HY-13992; CAS: 195514-80-8
Fludarabine	MedChemExpress	HY-B0069; CAS: 21679-14-1
Bentamapimod	MedChemExpress	HY-14761; CAS: 848344-36-5
YK-4-279	MedChemExpress	HY-14507; CAS: 1037184-44-3
YAP/TAZ inhibitor-1	TargetMol	T13364; CAS: 2093565-23-0
CCG-1423	MedChemExpress	HY-13991; CAS: 285986-88-1
Necrosulfonamide	Sigma-Aldrich	Cat# 480073; CAS: 432531-71-0
Yoda1	MedChemExpress	HY-18723; CAS: 448947-81-7
Critical commercial assays		
CellTiter-Glo® kit	Promega	G7571
ImmPACT DAB Peroxidase Substrate Kit	Vector	cat#SK-4105
Deposited data		
RNA-seq: Effect of L-MAT on HeLa cells (bulk, relative FPKM values)	This paper	GEO: GSE328527
RNA-seq: Expression profiles of B16F10, MCF7, HeLa and C2C12 cell lines (bulk, relative FPKM values)	This paper	GEO: GSE328536
Raw western blot data	This paper	Mendeley Data: https://doi.org/10.17632/73cbf9hvbp.1

(*Continued on next page*)

Continued

REAGENT or RESOURCE	SOURCE	IDENTIFIER
Experimental models: Cell lines		
HeLa sg-*MLKL*	This paper	N/A
HeLa sg-*STAT1*	This paper	N/A
HeLa sg-*PIEZO1*	This paper	N/A
C2C12 sg-*Mlkl*	This paper	N/A
C2C12 sg-*Stat1*	This paper	N/A
C2C12 sg-*Piezo1*	This paper	N/A
B16F10 sg-*Mlkl*	This paper	N/A
B16F10 sg-*Stat1*	This paper	N/A
B16F10 sg-*Piezo1*	This paper	N/A
C2C12-MLKL (1-178)-2*FKBP	This paper	N/A
B16F10-MLKL (1-178)-2*FKBP	This paper	N/A
Experimental models: Organisms/strains		
C57BL/6J mouse	Shanghai Lingchang Biotechnology Co., Ltd.	N/A
Oligonucleotides		
Primer: human MLKL Forward: AGGAGGCTAATGGGGAGATAGA; Reverse: TGGCTTGCTGTTAGAAACCTG	This paper	N/A
Primer: mouse MLKL Forward: AATTGTACTCTGGGAAATTGCCA; Reverse: TCTCCAAGATTCCGTCCACAG	This paper	N/A
Human PIEZO1 sgRNA sense oligo forward: CGCTTCAGCGGACTCTCGC	This paper	N/A
Mouse Piezo1 sgRNA sense oligo forward: TTGAGACACCTTCACCCAA	This paper	N/A
Human MLKL sgRNA sense oligo forward: ACTCTTCAAGGACGTGAAC	This paper	N/A
Mouse MLKL sgRNA sense oligo forward: GCACACGGTTTCCTAGACGC	This paper	N/A
Human STAT1 sgRNA sense oligo forward: TTGATCATCCAGCTGTGAC	This paper	N/A
Mouse Stat1 sgRNA sense oligo forward: TGGTTCGAGCTTCAGCAGC	This paper	N/A
Primer: human GAPDH Forward: CTGGGCTACACTGAGCACC; Reverse: AAGTGGTCGTTGAGGGCAATG	This paper	N/A
Primer: mouse GAPDH Forward: AGGTCGGTGTGAACGGATTTG; Reverse: TGTAGACCATGTAGTTGAGGTCA	This paper	N/A
Recombinant DNA		
lentiCRISPRv2-sg-human *MLKL*	This paper	N/A
lentiCRISPRv2-sg-human *STAT1*	This paper	N/A
lentiCRISPRv2-sg-human *PIEZO1*	This paper	N/A
lentiCRISPRv2-sg-mouse *Mlkl*	This paper	N/A
lentiCRISPRv2-sg-mouse *Stat1*	This paper	N/A
lentiCRISPRv2-sg-mouse *Piezo1*	This paper	N/A
pcDNA3.1-human MLKL-Flag	This paper	N/A
Software and algorithms		
Fiji	Schindelin et al.[62]	https://fiji.sc/
MetaMorph	Molecular Devices	https://www.moleculardevices.com
MATLAB	The MathWorks	https://www.mathworks.com

(*Continued on next page*)

Continued

REAGENT or RESOURCE	SOURCE	IDENTIFIER
DESeq2	Love et al.[63]	https://bioconductor.org/packages/DESeq2/
featureCounts	Liao et al.[64]	https://subread.sourceforge.net/featureCounts.html
HISAT2	Kim et al.[65]	https://daehwankimlab.github.io/hisat2/
NIS-Elements	Nikon Instruments	https://www.microscope.healthcare.nikon.com/products/software
GraphPad Prism 9	Dotmatics	https://www.graphpad.com/

EXPERIMENTAL MODEL AND STUDY PARTICIPANT DETAILS

Animals

Wild-type C57BL/6J mice (approximately 6 weeks old, male) were purchased from Shanghai Lingchang Biotechnology and used for the lung metastatic melanoma model. Mice were maintained under specific pathogen-free (SPF) conditions with free access to food and water under a 12-h light/dark cycle. All animal experiments were performed in accordance with institutional guidelines and were approved by the Institutional Animal Care and Use Committee of the Center for Excellence in Molecular Cell Science, Chinese Academy of Sciences.

For the lung metastatic melanoma model, B16F10 cells were washed three times with PBS and filtered through a 70-μm cell strainer. A total of 1 x 10^6 cells were intravenously injected into the tail vein of C57BL/6J mice. Mice were monitored regularly for body weight, general health, and signs of tumor-related distress. Animals were euthanized at 14 days post-injection for subsequent analysis or earlier if humane endpoint criteria were reached. For measurable tumor lesions, a tumor burden exceeding 1,500 mm^3 was considered a humane endpoint. Other humane endpoints included severe deterioration in general condition, substantial body weight loss, impaired mobility or feeding, respiratory distress, or other signs of significant suffering.

Cell Lines

HeLa cells were a gift from Matthieu Piel's laboratory. HeLa, HT-29, HCT116, BT549, MCF-7, 293T, C2C12, $MLKL^{1-178}$-2×FKBP-C2C12, B16F10, $MLKL^{1-178}$-2×FKBP-B16F10 were cultured in Dulbecco's modified Eagle's medium (DMEM, gibco, 6123084) supplemented with 10% fetal bovine serum (FBS, GIBCO, Cat#10099141) and 100 units/mL penicillin/streptomycin. Cells were cultured at 37°C in a 5% CO_2 incubator. All cell lines were tested to be mycoplasma-negative by the standard PCR method.

METHOD DETAILS

Reagents

Trypsin (#25200072) was purchased from ThermoFisher Scientific. CellTiter-Glo Luminescent Cell Viability Assay Kit (Promega, cat#7573). B/B Homodimerizer (MCE, AP20187). Tacrolimus (MCE, FK506). SYTOX Green (Invitrogen, 100 nM). GsMTx4 (MCE, HY-P1410). Yoda1 (MCE, HY-18723). Fludarabine (MCE, HY-B0069). Bentamapimod (MCE, HY-14761). YK-4-279 (MCE, HY-14507). YAP/TAZ inhibitor-1 (TargetMol, T13364). CCG-1423 (MCE, HY-13991). N-Acetylcysteine (MCE, HY-B0215). BAPTA-AM (MCE, HY-100545). Necrosulfonamide (Sigma-Aldrich, Cat# 480073). Anti-Flag antibody (Sigma-Aldrich, Cat#A8592). Anti-M Mlkl (Abgent, Cat#AP14272b). Anti-Mlkl (Cell Signaling Technology, Cat#14993). Anti-phospho MLKL (Abcam, Cat#ab187091). Anti-STAT1 (Cell Signaling Technology, Cat#9172). Anti-Phospho STAT1 (Cell Signaling Technology, Cat#9167). Anti-PIEZO1 (HUABIO, Cat#M1005-2). Anti-RIPK3 (Abcam, Cat#ab226297). Anti-GAPDH antibody (ABclonal, Cat#AC033). Anti-Cox IV (Proteintech, Cat#11242-1-AP). Anti-β-actin (ABclonal, Cat#AC004).

SYTOX Green/PI Staining Assay

SYTOX Green/PI is added to the cell culture medium to trace the plasma membrane breakdown during microscopic imaging. The intranuclear DNA fluorescent signal of SYTOX Green/PI indicated the membrane leakage.

ATP Assay

Cell viabilities (the intracellular ATP levels of the remaining cells) were measured with the CellTiter-Glo Luminescent Cell Viability Assay Kit according to the manufacturer's instructions. Necroptosis was quantified by subtracting the cell viability from the initial total cell viability.

Acquisition of MLKL-Activated Survivor Cells

hMLKL1-178-2×FKBP-C2C12 or B16F10 cells were cultured in DMEM supplemented with 10% FBS and 1% penicillin/streptomycin. MLKL dimerization was induced by adding 10 nM dimerizer until cell detachment occurred. Subsequently, 10 μM Tacrolimus (Tac), a dimerizer competitor, was added to inhibit further MLKL activation. The cells were then trypsinized, resuspended in fresh DMEM with 10% FBS and 1% penicillin/streptomycin, and used in the MAT-induction assay and B16F10 lung metastasis model (in Figures 3 and 4).

Immunohistochemistry Staining

Isolated B16F10 tumors were fixed overnight in 4% paraformaldehyde (PFA), dehydrated through a graded ethanol series and xylene, and embedded in paraffin. Sections (5 μm thick) were deparaffinized, rehydrated, and treated with 3% hydrogen peroxide to block endogenous peroxidase activity. Antigen retrieval was performed in 10 mM citric acid buffer (pH 6.0) containing 0.05% Tween 20. Subsequently, sections were incubated in 3% H_2O_2 at room temperature overnight to bleach endogenous melanin pigment. Sections were blocked with 4% normal goat serum and incubated overnight at 4°C with an MLKL antibody. After washing with TBST, the sections were incubated with HRP-conjugated secondary antibodies for 1 hour at room temperature. Signal development was performed using the ImmPACT DAB Peroxidase Substrate Kit (Vector, cat#SK-4105), followed by counterstaining with hematoxylin. The sections were then dehydrated through ethanol and xylene, mounted with mounting medium, and images were captured using the BX53 microscope (Olympus).

Immunofluorescence staining

Cells were seeded onto coverslips in a 6-well plate. Following L-MAT treatment, the cells were fixed on the coverslips with 4% paraformaldehyde for 20 min. After washing with PBS, the cells were permeabilized using 0.25% Triton X-100 for 20 min, blocked with 5% bovine serum albumin for 1 h at room temperature, and incubated with primary antibodies overnight at 4 °C. This was followed by incubation with secondary antibodies for 2 h at room temperature. After thorough washing with PBST, the cells were counterstained with DAPI for 10 min to label the nuclei and examined using a confocal microscope.

Fabrication of the Cell Confiner

The multi-well cell confiners used for MAT induction in this study were developed in our lab and have been previously described in detail.[6,66] Briefly, micropillar patterns on glass slides were obtained from custom-made molds on silicon wafers, which were fabricated using standard photolithography with SU-8 2005 photoresist, following the manufacturer's protocol. The molds were then treated with trimethylchlorosilane (TMCS) for 3 minutes by evaporation. Subsequently, 12 mm diameter glass coverslips were pressed onto the SU-8 molds, which were coated with Polydimethylsiloxane (PDMS) RTV615 (Momentive Performance Materials) at an 8:1 base-to-curing agent ratio to form the confining slides. These were baked on a 95°C hot plate for 15 minutes, and the resulting PDMS pillar structures were peeled off using a small amount of isopropanol.

The fabrication process continued as follows: 1) Large PDMS pads, prepared by mixing PDMS (A:B = 35:1) in a custom-made mold, were attached to the center of each well's cover lid using 100 μm thick gel-film sheets (Gel-Pak). 2) The confining slides were then modified with 0.1 mg/mL pLL(20)-g[3.5]-PEG(2) (PLL-PEG, SuSoS) in 10 mM HEPES buffer for 1 hour. 3) Before cell loading, the confining slides were equilibrated in cell culture medium, then positioned on the PDMS pads.

Live Cell Imaging

Phase and fluorescence time-lapse imaging were performed using a 20× air phase objective on a Leica inverted microscope equipped with a CMOS camera, controlled by MetaMorph software (Universal Imaging). For myosin retrograde flow imaging, Total Internal Reflection Fluorescence (TIRF) microscopy was conducted on an Eclipse Ti inverted microscope (Nikon) with a 100× oil objective and a Prim 95B camera, controlled by NIS-Elements software (Nikon). All microscopes were equipped with an incubation chamber (Okolab) maintaining a temperature of 37°C and 5% CO_2. Image acquisition and analysis were performed using ImageJ and MATLAB software.

Image Analysis

Cell migration analysis was conducted using ImageJ and MATLAB. For each tracked cell, individual trajectories were extracted and manually clustered based on morphology using the Manual Tracking plugin in TrackMate (ImageJ). The mean migration speed was calculated using a custom MATLAB script (MathWorks, USA). Actin retrograde flow distributions were analyzed from registered time-lapse TIRF images of representative cells. Kymographs were generated using an ImageJ plugin and processed to remove horizontal and vertical artifacts with ImageJ Fourier transform tools. The speed of actin retrograde flow was determined by measuring the slope of the actin trajectory in the kymographs.

Transcriptomic analysis of HeLa cells under L-MAT

For bulk RNA-seq analysis, HeLa Kyoto cells were seeded in six-well plates at a density of 200,000 cells per well. For each of three independent biological replicates, two plates of cells were subjected to mechanical confinement for approximately 8 hours using six-well static non-adhesive confiners with a height of 3 μm, while cells on two additional plates were maintained as no MAT induction as controls. Then cells from both plates of the same condition were pooled to generate samples of approximately 240,000 cells each and collected in TRIzol. Library preparation and sequencing were performed by OE Biotech Co., Ltd.

RNA-seq raw reads of HeLa cells under L-MAT were first subjected to quality control and low-quality reads were removed. High-quality reads were aligned to the reference genome with HISAT2 (version 2 2.2.1), and the resulting alignments were saved in BAM format and sorted. Gene-level read counts were then quantified using featureCounts (version 2.0.1) against the reference annotation to generate a count matrix. Differential expression analysis was performed in R (version 4.3.1) with the DESeq2 package (version DESeq2): counts were normalized and statistical testing was carried out under a negative-binomial model. Genes were considered differentially expressed if the adjusted P-value (FDR) was < 0.05 and the fold-change criterion was also satisfied. A volcano plot was used to visualize the overall distribution of differentially expressed genes.

Gene Ontology Enrichment Analysis

Differentially expressed genes (DEGs) were identified using DESeq2 v1.46.0 ($|\log2FC| > 0.58$, $p < 0.05$). Gene Ontology (GO) enrichment analysis was performed using clusterProfiler v4.6.0 in R v4.3.1. Biological process terms related to cell migration were specifically screened and identified. Both circle plots and gene–pathway chord diagrams were constructed using the GOplot package v1.0.2. Complete GO term annotations and statistical parameters are provided in Tables S1, S2, and S3.

Transwell Assay

Migration assays were conducted in 24-well plates with 3- or 12-μm pore size Transwell inserts (BD Biosciences). A total of 680 μl of culture medium was added to the lower chamber of each well. For each condition, 4×10^5 cells suspended in serum-free medium were added to the upper chamber. After incubation at 37°C and 5% CO_2 for 24 hours, non-migrated cells remaining on the upper surface of the membrane were gently scraped off. The migrated cells on the lower surface of the membrane were then stained with Hoechst for quantification.

Microfluidic Chip Assay

Soft photolithography and replica molding were used to fabricate PDMS-based microchannel devices of different dimensions.[67] Briefly, a darkfield, chrome-coated glass mask was printed with microtrack geometries designed in K-Layout and then transferred to a wafer using soft photolithography to obtain a custom-made mold. Microchannels were fabricated from polydimethylsiloxane (PDMS) following previously described protocols.[68,69] PDMS was mixed at a 10:1 ratio and cast into a custom-made mold with microchannels of 4 or 8 μm width and 10 μm height. After curing at 65°C for 12 hours, the PDMS was peeled from the mold, cut into 10 × 10 mm pieces to fit standard 35-mm glass-bottom dishes, and plasma activated. The activated PDMS pieces were bonded to the glass-bottom dishes and further strengthened by heating at 65°C for 20 minutes. The microchannels were incubated with 25 μg/ml fibronectin at room temperature for 1 hour, followed by washing with PBS. They were then incubated with the appropriate culture medium for at least 1 hour at 37°C in 5% CO_2 prior to cell loading. A 30 μl drop of cell suspension was added to the microchannel inlets and allowed to settle for approximately 30 minutes. Finally, additional medium was added to the dish to maintain cell viability for up to 48 hours.

SRT Dataset and Bioinformatics Analyses

To investigate the role of physical confinement in shaping cancer cell behavior and driving tumor progression, we analyzed two publicly available Spatial RNA-Seq (SRT) datasets: one from breast cancer and another from colorectal cancer with liver metastasis. We used stKeep, a multi-model heterogeneous approach developed in our previous study,[44] to identify spatial domains and denoise gene expression data. To assess the relationship between MLKL expression and cell density across different malignancy groups, we manually annotated regions of uniform circular size using LabelMe software.[70] For each region, we calculated the mean expression of spots and estimated cell density using ImageJ. Additionally, we quantified the gene activity score of the STAT1-targeted gene set, curated from the published ChIP-chip database,[71] using the 'AddModuleScore' function in the Seurat package.[72]

The raw spatial transcriptomics data for human invasive ductal carcinoma (IDC) breast cancer sample is publicly available at the 10× Genomics Website (https://support.10xgenomics.com/spatial-gene-expression/datasets). The raw spatial transcriptomics data for colon cancer liver metastasis sample is available at The National Omics Data Encyclopedia (https://www.biosino.org/node/project/detail/OEP001756).

QUANTIFICATION AND STATISTICAL ANALYSIS

All images were processed with ImageJ. Quantification and statistical analyses were performed using GraphPad Prism (v[9], Dotmatics). Data are presented as mean ± SD. The exact value of n, definition of center and dispersion, and statistical tests used are indicated in the corresponding figure legends. Comparisons between two groups were performed using an unpaired two-tailed Student's t-test with Welch's correction. Comparisons among multiple groups were performed using one-way or two-way ANOVA followed by Šidák's multiple-comparisons test, or Tukey's multiple-comparisons test for single-factor designs. Normalized values were compared with a theoretical value of 1 using a one-sample t-test. Correlations were assessed using Pearson's correlation coefficient (r). Statistical significance was defined as $P < 0.05$ (*), $P < 0.01$ (**), $P < 0.001$ (***), and $P < 0.0001$ (****); ns, not significant.

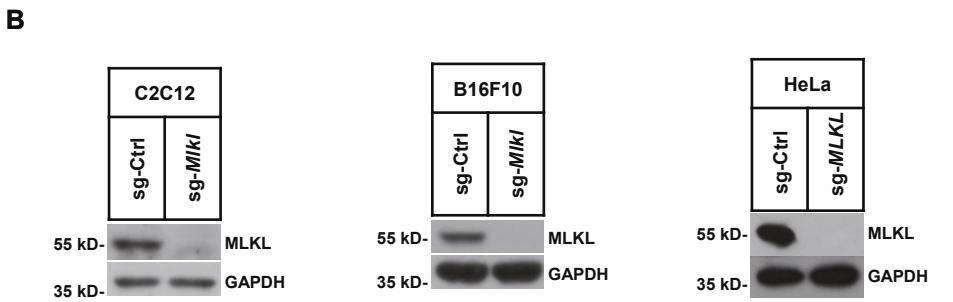
Developmental Cell, Volume *61*

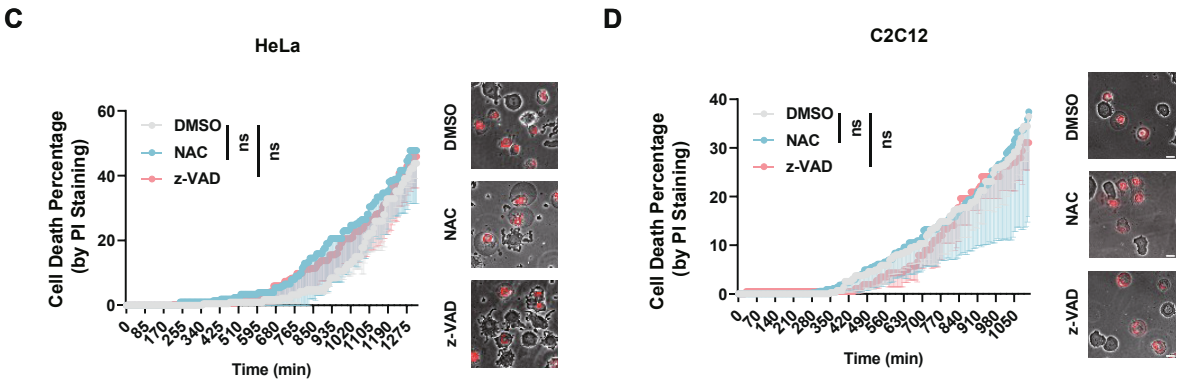
Supplemental information

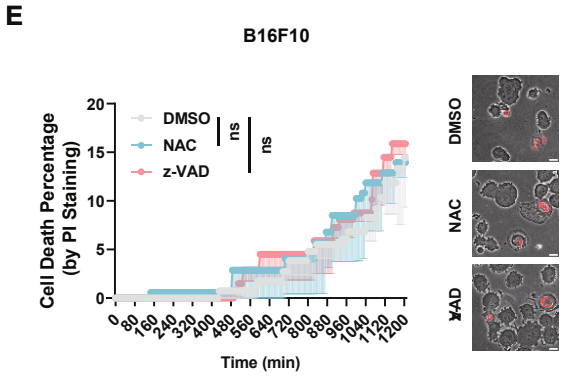
Long-term confinement triggers RIPK3-independent necroptosis in amoeboid cancer cells to shape tumor evolution

Wei Zhang, Ya-Jun Wang, Chunman Zuo, Junyi He, Xuying Ma, Haoran Wu, Bao-Qiong Lan, Dehui Kong, Luonan Chen, Gang Wei, Na Yang, Yuandi Fu, Dan Liu, Yan-Jun Liu, and Liming Sun









Supplementary Figure 1 | Validation of MLKL-dependent necroptosis following L-MAT across cell lines and controls, related to Figure 1.

Supplementary Figure 1 | Validation of MLKL-dependent necroptosis under L-MAT across cell lines and controls, related to Figure 1.

(A) Representative immunohistochemical staining of MLKL in subcutaneous tumors formed by control (sg-Ctrl) or *Mlkl*-knockout (sg-*Mlkl*) B16F10 cells. MLKL signal (brown) is counterstained with hematoxylin (blue). Red dashed lines demarcate high MLKL signal zones; green dashed lines demarcate low MLKL signal zones.

(B) Quantification of cell density in high versus low MLKL signal zones (upper panel). Cell density (cells/mm²) was determined from defined- size imaging fields using watershed segmentation with size- range exclusion by imageJ, followed by manual verification. Tissue slice thickness was 5 μm.

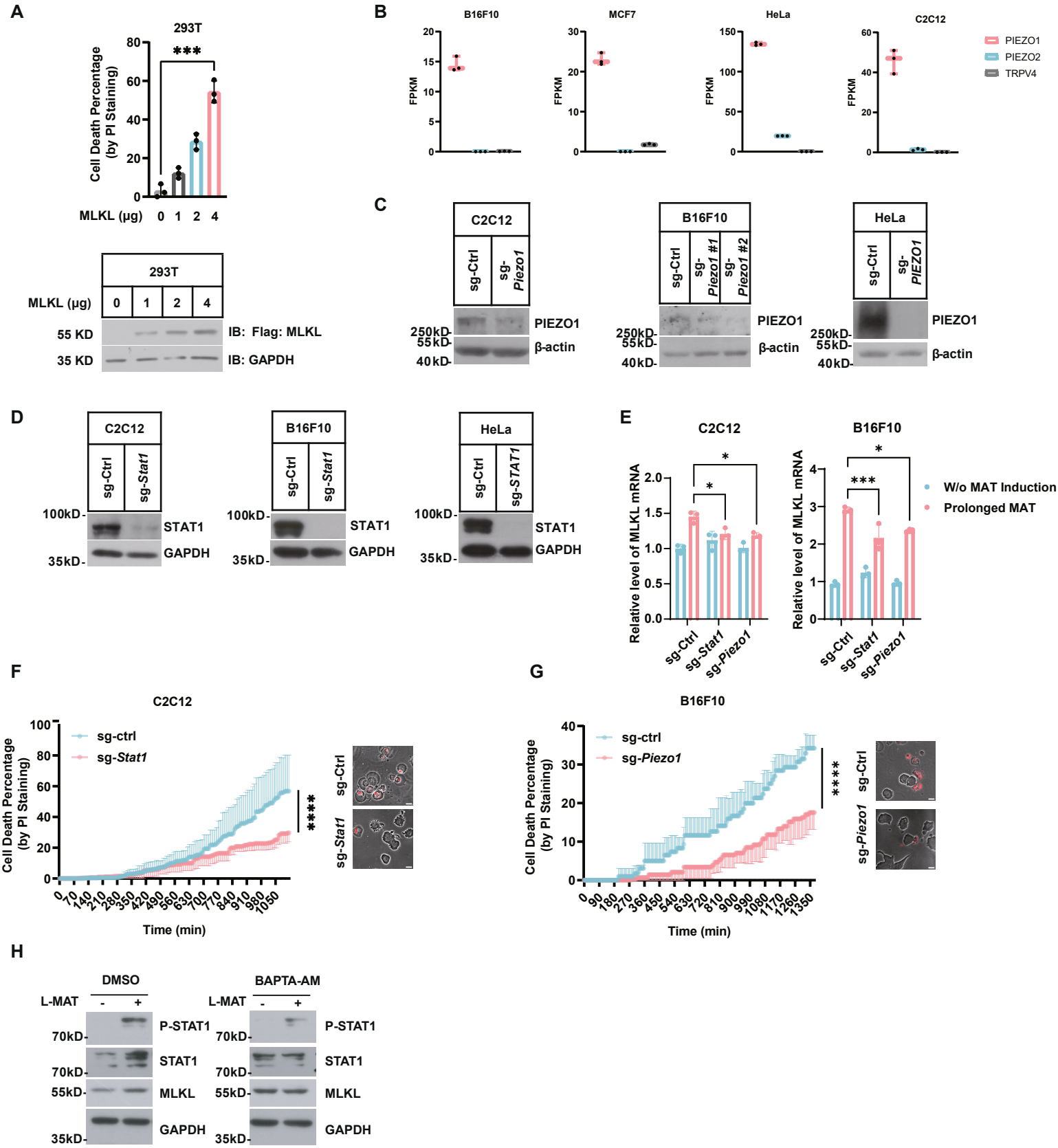
(C) Pearson correlation analysis between cell density and MLKL intensity from (A) (lower panel).

(D)GO enrichment analysis revealed that differentially expressed genes in L-MAT–tre ated HeLa cells were significantly enriched in pathways governing core cellular behav ior & signaling, including cell death and cell adhesion.

(E) Immunoblot analysis confirming MLKL knockout efficiency in indicated cell lines.

(F–H) Neither ROS inhibition nor apoptosis inhibition prevents L-MAT-induced cell death. Time course quantification of cell death following treatment with the ROS inhibitor N-acetylcysteine (NAC) or the apoptosis inhibitor z-VAD (20 μM) in HeLa (E), C2C12 (F), and B16F10 (G) cells. Representative images show PI-positive cells indicating plasma membrane rupture. Scale bar, 20 μm.

Bars show **mean ± SD**; individual dots represent single cells. Statistical analysis was performed using unpaired two-tailed Student's t-test with Welch's correction. ****P < 0.0001; ns, not significant. All experiments were repeated ≥3 independent times with consistent results; statistical analysis was conducted on pooled replicate data.



Supplementary Figure 2 | Piezo1–STAT1 signaling drives MLKL upregulation and necroptotic cell death following L-MAT, related to Figure 2.

Supplementary Figure 2 | Piezo1–STAT1 signaling drives MLKL upregulation and necroptotic cell death following L-MAT, related to Figure 2.

(A) MLKL overexpression is sufficient to induce cell death. HEK293T cells were transfected with increasing doses of MLKL-encoding plasmid. Upper panel: cell viability assessed by ATP luminescence assay. Lower panel: immunoblot analysis of MLKL expression.

(B) RNA-seq analysis indicates that *PIEZO2* and *TRPV4* are minimally expressed across the cell lines examined, suggesting they do not contribute to L-MAT-induced necroptosis.

(C) Immunoblot analysis confirming PIEZO1 knockout efficiency in the indicated cell lines.

(D) Immunoblot analysis confirming STAT1 knockout efficiency in the indicated cell lines.

(E) *Piezo1* and *Stat1* are required for L-MAT-induced *Mlkl* upregulation in murine cells. *Mlkl* mRNA levels were quantified by RT-qPCR in control, *Stat1*-knockout, or *Piezo1*-knockout C2C12 and B16F10 cells following L-MAT induction. All samples were measured within the same batch. Expression levels were normalized to *Gapdh* and presented relative to the control genotype (sg-*Ctrl*) without MAT induction as a shared reference, allowing direct statistical comparisons across all genotypes and conditions.

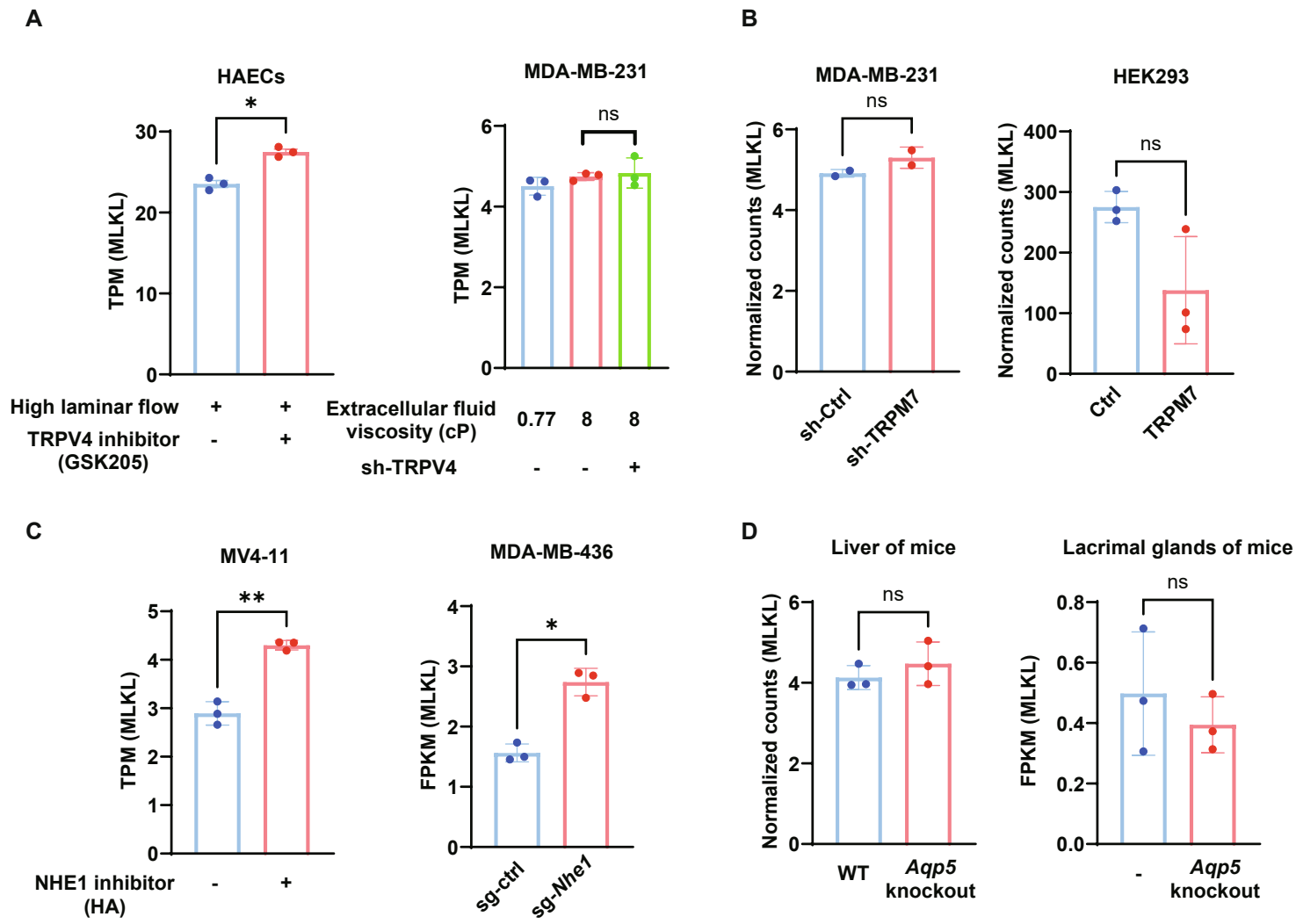
(F) *Stat1* knockout reduces L-MAT-induced cell death in C2C12 cells. Time course analysis of cell death in control (sg-Ctrl) or *Stat1*-knockout (sg-*Stat1*) C2C12 cells under MAT induction. Representative images show PI-positive cells indicating plasma membrane rupture. Scale bar, 20 μm.

(G) *Piezo1* knockout reduces L-MAT-induced cell death in B16F10 cells. Time course analysis of cell death in control (sg-Ctrl) or *Piezo1*-knockout (sg-*Piezo1*) B16F10 cells under MAT induction. Representative images show PI-positive cells indicating plasma membrane rupture. Scale bar, 20 μm.

(H) Calcium chelation suppresses L-MAT-induced STAT1 activation and MLKL upregulation. HeLa cells were pretreated with the intracellular calcium chelator BAPTA-AM (5 μM) or DMSO for 2 h, followed by L-MAT induction. Immunoblot analysis was performed to examine the levels of phosphorylated STAT1 (P-STAT1), total STAT1, and MLKL following L-MAT treatment. GAPDH served as a loading

control.

Bars depict mean ± SD; dots represent individual replicates or single cells, depending on assay. Statistical analysis was performed using one-way ANOVA followed by Tukey's multiple comparisons test for comparisons in (A), and two-way ANOVA followed by Sidak's multiple comparisons test for comparisons in (E, F, and G). *P < 0.05, ***P < 0.001, ****P < 0.0001. All experiments were repeated at least three independent times with consistent results; statistics were calculated from pooled replicate data.



Supplementary Figure 3 | Inhibition or knockout of other mechanosensitive ion channels does not inhibit MLKL transcription, related to Figure 2.

Supplementary Figure 3 | Inhibition or knockout of other mechanosensitive ion channels does not inhibit MLKL transcription, related to Figure 2.

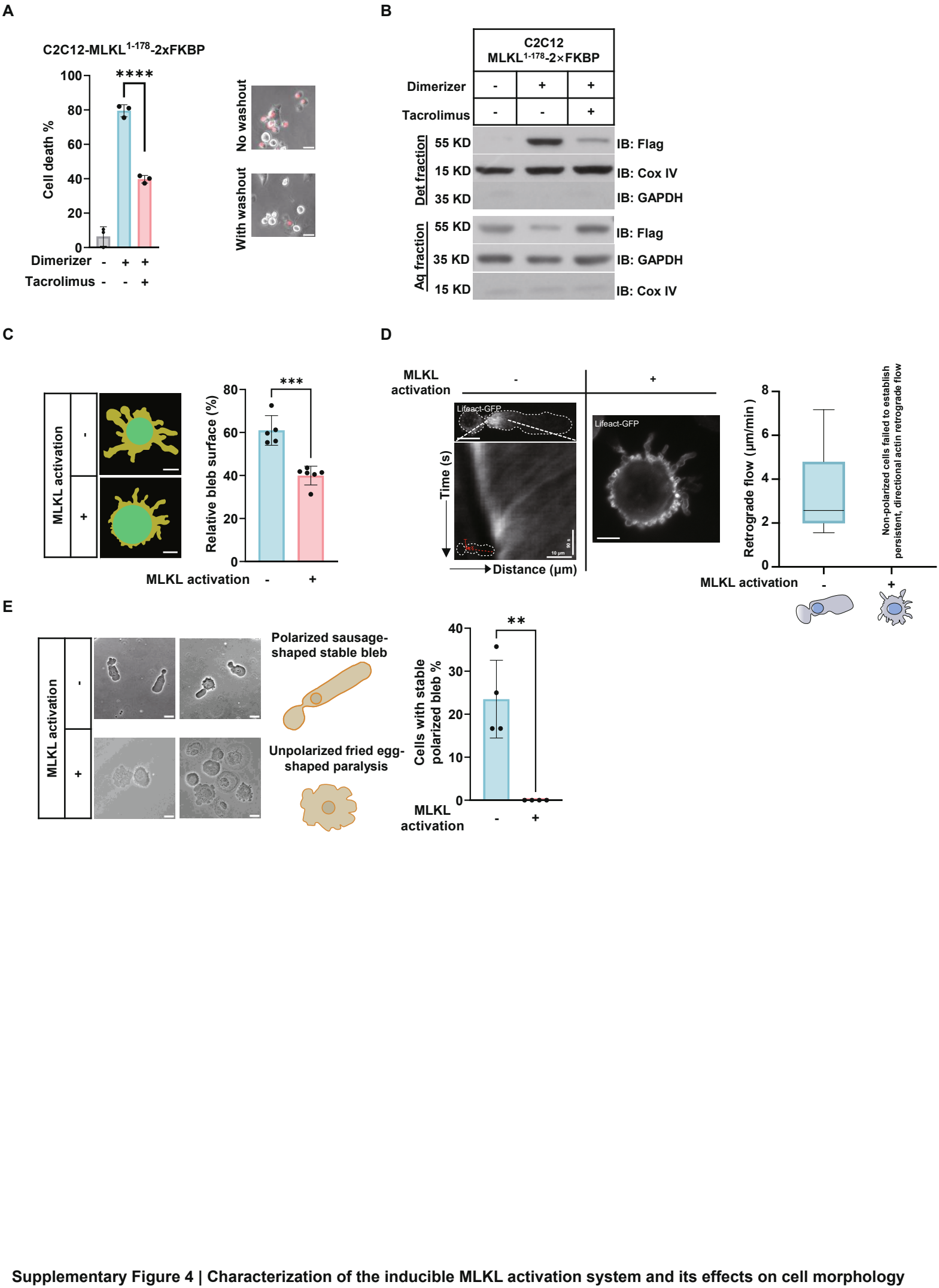
(A) TRPV4 inhibition does not inhibit MLKL transcription. Left panel: MLKL transcript levels (TPM) in human aortic endothelial cells (HAECs) under laminar flow treated with the TRPV4 antagonist GSK205 versus control (GSE255770). Right panel: MLKL transcript levels (TPM) in sh-Ctrl versus sh-*TRPV4* MDA-MB-231 cells cultured at 0.77 cP or 8 cP viscosity (GSE203651).

(B) TRPM7 modulation does not affect MLKL expression. Left panel: MLKL expression (normalized signal intensity) following *TRPM7* knockdown (GSE63956). Right panel: MLKL expression (normalized signal intensity) in control versus *TRPM7*-overexpressing HEK cells (GSE23102).

(C) NHE1 inhibition or knockout does not inhibit MLKL expression. Left panel: MLKL transcript levels (TPM) in MV4-11 cells treated with NHE1 inhibitor for 48 hours (GSE247175). Right panel: MLKL transcript levels (TPM) in control versus *NHE1*-knockout MDA-MB-436 cells (GSE270232).

(D) *Aqp5* knockout does not affect MLKL expression. Left panel: MLKL transcript levels (normalized counts) in liver tissue from wild-type versus $Aqp5^{-/-}$ mice post-partial hepatectomy (PHx) (GSE284995). Right panel: MLKL transcript levels (FPKM) in lacrimal gland tissue from wild type versus $Aqp5^{-/-}$ mice (GSE149832).

n represents the number of biological samples/groups in each dataset as deposited in GEO. Bars indicate mean ± SD; individual dots represent values from each biological replicate/sample. Statistical analysis was performed using unpaired two-tailed Student's t-test with Welch's correction. *P < 0.05, **P < 0.01, ns, not significant. Statistical computations used all available replicate values from the original datasets; no representative subset was used.



Supplementary Figure 4 | Characterization of the inducible MLKL activation system and its effects on cell morphology and cytoskeletal dynamics during MAT, related to Figure 3.

Supplementary Figure 4 | Characterization of the inducible MLKL activation system and its effects on cell morphology and cytoskeletal dynamics during MAT, related to Figure 3.

(A) Necroptosis can be halted by competitive washout of the MLKL dimerizer, enabling extended monitoring of migration behavior. C2C12-MLKL(1–178)-2×FKBP cells were treated with 10 nM dimerizer (AP20187) to induce MLKL activation until cell detachment, followed by 10 μM tacrolimus to inhibit further MLKL activation. Cell viability was assessed by ATP levels during necroptosis.

(B) MLKL membrane translocation is attenuated by dimerizer inhibition. Cell lysates were incubated at 30°C, and aqueous and detergent phases were separated. MLKL distribution between cytoplasm and plasma membrane fractions was analyzed by immunoblotting.

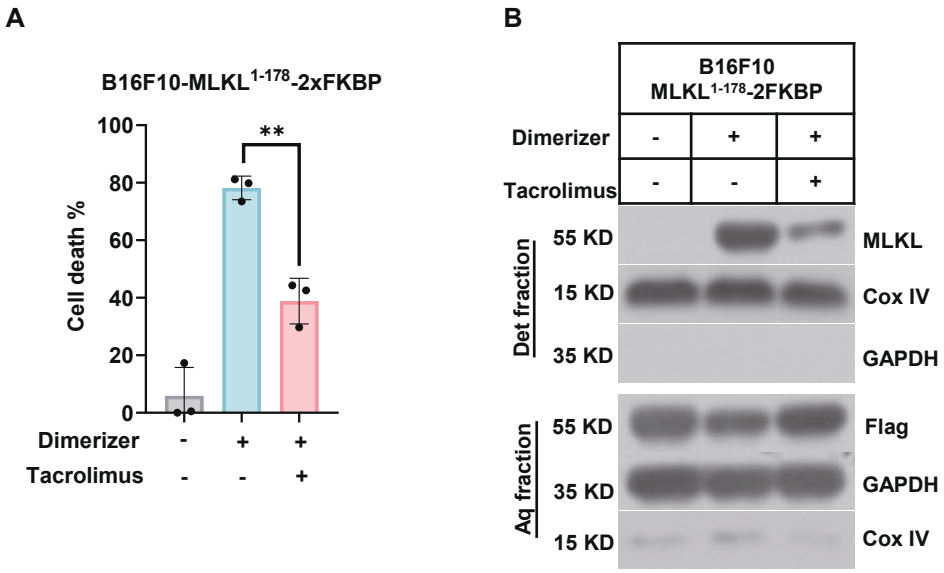
(C) MLKL-activated cells exhibit reduced blebbing activity following MAT induction. Left panel: representative images of blebbing. Right panel: quantification of bleb surface area (yellow in schematic) relative to total cell surface (green in schematic). Scale bar, 10 μm. n = 147 (non-activated) and 109 (MLKL-activated) cells.

(D) MLKL activation abolishes retrograde actin flow. Left: Representative TIRF microscopy images of actin dynamics in C2C12 cells expressing Lifeact-EGFP following MAT induction. Kymographs reveal strong retrograde flow of intracellular F-actin in non-activated cells, whereas MLKL-activated, unpolarized cells show no detectable retrograde actin flow. White dashed lines indicate cell outlines; red dashed lines indicate regions used to generate kymographs. Horizontal bars, 10 μm; vertical bars, 90 sec. Retrograde actin flow velocity was quantified from the actin kymographs shown on the left. Upon MLKL activation, cells lost polarity and failed to establish persistent directional retrograde actin flow, precluding reliable quantification of retrograde flow velocity.

(E) MLKL-activated cells fail to polarize and adopt unpolarized, fried-egg-shaped morphology following MAT induction. Non-activated cells exhibit polarized, sausage-shaped morphologies with stable blebs, whereas MLKL-activated cells form unpolarized, fried-egg-shaped structures. Left panels: representative images. Middle panels: schematic of cell morphology. Right panel: quantification. Scale bar, 20 μm. n = 73 (non-activated) and 72 (MLKL-activated) cells.

Bars indicate mean ± SD; individual dots represent each tracked cell or biological replicate as appropriate. Statistical analysis was performed using unpaired two-tailed Student’s t-test with Welch’s correction. **P < 0.01, ***P < 0.001, ****P < 0.0001,

ns, not significant. All experiments repeated at least three independent times with consistent results; statistics calculated from pooled replicate data.



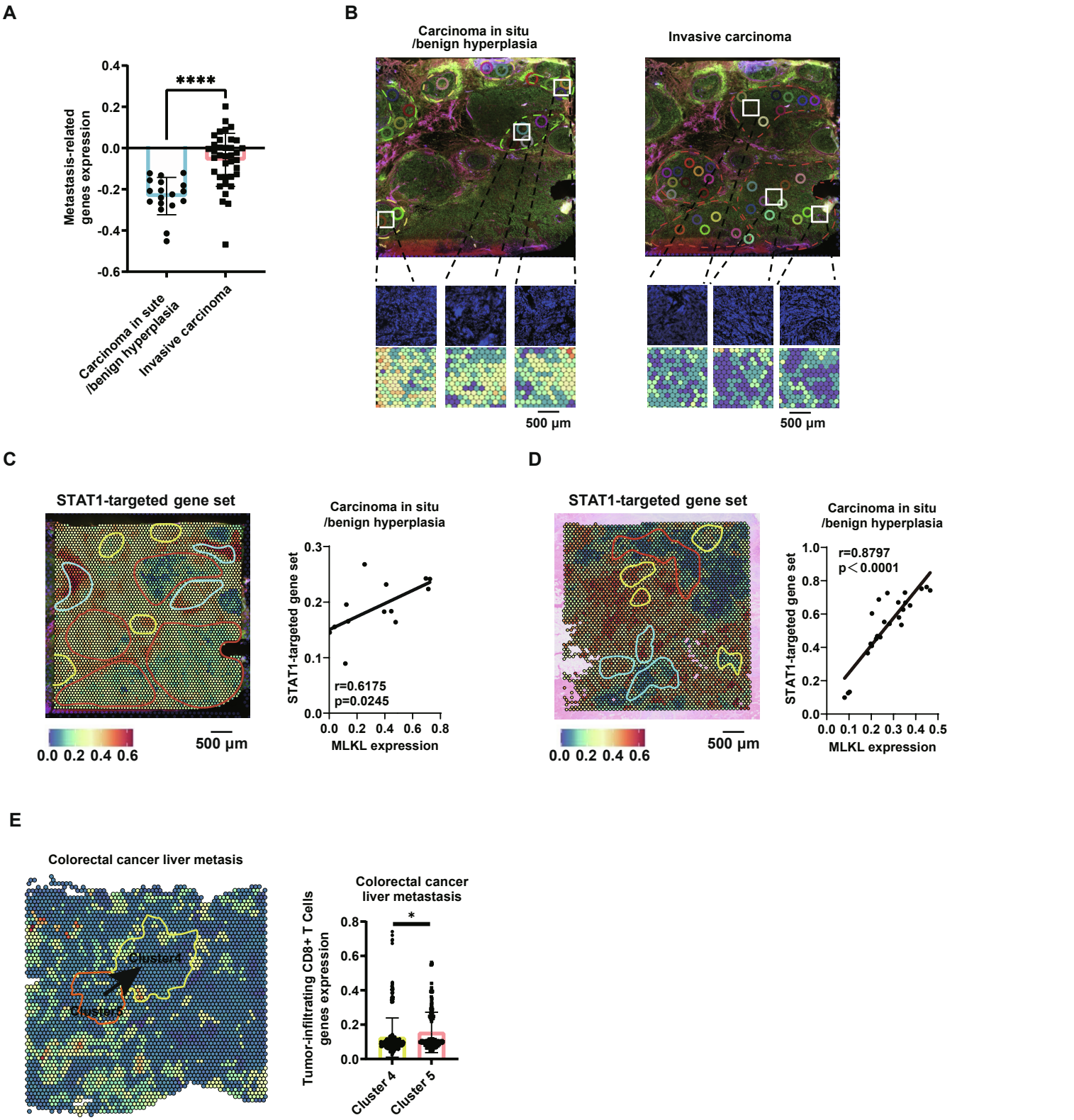
Supplementary Figure 5 | Validation of dimerizer washout strategy for controlled MLKL activation in B16F10 cells, related to Figure 4.

Supplementary Figure 5 | Validation of dimerizer washout strategy for controlled MLKL activation in B16F10 cells, related to Figure 4.

(A) Necroptosis is halted by competitive washout of the MLKL dimerizer. B16F10-MLKL(1–178)-2×FKBP cells were treated with 10 nM dimerizer (AP20187) to induce MLKL activation until cell detachment, followed by 10 μM tacrolimus to inhibit further MLKL activation. Cell viability was assessed by measuring ATP levels.

(B) Dimerizer inhibition attenuates MLKL membrane translocation. Cell lysates were incubated at 30°C, and aqueous and detergent phases were separated. MLKL distribution between cytoplasm and plasma membrane fractions was analyzed by immunoblotting.

Bars show mean ± SD; individual dots represent single cells. Statistical analysis was performed using unpaired two-tailed Student's t-test with Welch's correction. **P < 0.01. All experiments were repeated ≥3 independent times with consistent results; statistical analysis was conducted on pooled replicate data.



Supplementary Figure 6 | Additional spatial transcriptomic analyses of MLKL expression and tumor microenvironment in human cancers, related to Figure 5.

Supplementary Figure 6 | Additional spatial transcriptomic analyses of MLKL expression and tumor microenvironment in human cancers, related to Figure 5.

(A) Correlation of metastasis-related gene expression within polyclonal lesions in the IDC (Luminal B) breast cancer patient sample. Spatial expression of breast cancer metastasis related genes in carcinoma in situ/benign hyperplasia and invasive carcinoma of IDC tissue. List of breast cancer metastasis related genes were referenced from GeneCards database (https://www.genecards.org/Search/Keyword?queryString=breast%20cancer%20metastasis&sections=pathways).

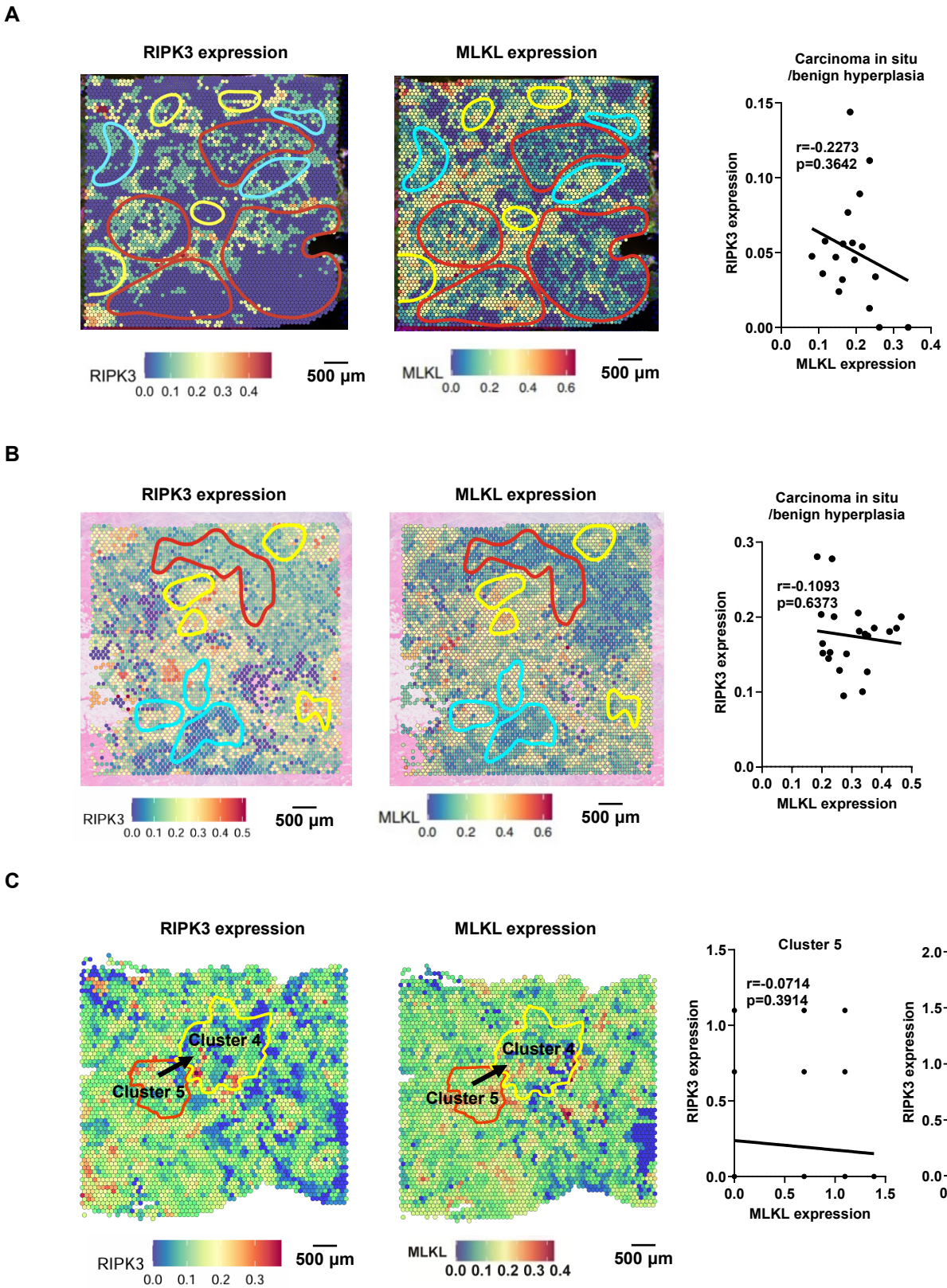
(B) Quantification of cell density and spatial MLKL expression in different zones. Circles represent selected fields for quantification analysis. DAPI staining (nuclei) was used for cell number quantification. Detailed analysis is provided in the Methods section.

(C) Spatial expression of MLKL and STAT1-targeted gene set in an invasive ductal carcinoma (IDC) breast cancer sample. Left: spatial gene expression maps of the STAT1-targeted gene set and MLKL. Right: Pearson correlation analysis reveals significant co-expression of the STAT1-targeted gene set and MLKL in the less aggressive ductal carcinoma in situ (DCIS) and benign hyperplasia regions.

(D) Spatial expression of MLKL and STAT1-targeted gene set in an FFPE-preserved breast cancer sample. Left: spatial gene expression maps of the STAT1-targeted gene set and MLKL. Right: Pearson correlation analysis reveals significant co-expression of the STAT1-targeted gene set and MLKL in the less aggressive ductal carcinoma in situ (DCIS) regions (#1 and #2).

(E) Spatial expression of tumor-infiltrating $CD8^+$ T cell-expressing genes in colorectal cancer liver metastasis tissue based on stKeep spatial clustering analysis. Left: spatial gene expression map. Right: quantification of tumor-infiltrating $CD8^+$ T cell gene expression across different regions.

n denotes independent spatial regions of interest (ROIs) within each tissue sample; numbers of ROIs for each comparison are detailed in Methods. Bars represent mean ± SD values across ROIs; each dot corresponds to a single ROI measurement. Unpaired two-tailed Student's t-test with Welch's correction. ****$P < 0.0001$. Analyses were conducted on all available ROIs pooled across ≥3 independent experiments or independent patient samples, ensuring that no single experiment was used as sole representation.



Supplementary Figure 7 | Comparison of MLKL and RIPK3 expression pattterns across human cancers, related to Figure 5.

Supplementary Figure 7 | Comparison of MLKL and RIPK3 expression patterns across human cancers, related to Figure 5.

(A) Spatial expression of RIPK3 and MLKL in an invasive ductal carcinoma (IDC) breast cancer sample. Left, spatial gene expression maps of RIPK3 and MLKL. Overall, RIPK3 expression is low throughout the tumor, particularly in the invasive carcinoma region, where MLKL expression is also relatively low. Right, Pearson correlation analysis of RIPK3 and MLKL expression in the less aggressive ductal carcinoma in situ (DCIS) and benign hyperplasia regions shows no significant correlation.

(B) Spatial expression of RIPK3 and MLKL in an FFPE-preserved breast cancer sample. Left, spatial gene expression maps of RIPK3 and MLKL. RIPK3 expression remains low, particularly within the invasive carcinoma region. Right, Pearson correlation analysis of RIPK3 and MLKL expression in the less aggressive ductal carcinoma in situ (DCIS) regions (#1 and #2) shows no significant correlation.

(C) Spatial expression of RIPK3 and MLKL in colorectal cancer with liver metastasis analyzed by stKeep-based spatial clustering. Left, spatial gene expression maps of RIPK3 and MLKL. Right, Pearson correlation analysis of RIPK3 and MLKL expression in the primary colorectal tumor (cluster 5) and liver metastatic lesion (cluster 4) shows no significant correlation.

Statistical significance for group comparisons was determined using an unpaired two-tailed Student's t-test with Welch's correction. Correlations were analyzed using the Pearson correlation coefficient.

Supplementary Table 1: GO Enrichment Analysis of L-MAT-induced HeLa Cells (related to Figure 3F)

GO ID	GO Term	Ontology	Category	Gene Ratio	Rich Factor	p-value	FDR (q-value)	z-score	Fold Enrichment	Contributing Genes
GO:0070507	regulation of microtubule cytoskeleton organization	BP	BP	136/11067		1.16625549230122e-12	2.61895970200975e-11			STMN1/STIL/PRKAA2/PATJ/SASS6/GPSM2/WDR47/PSRC1/PDE4DIP/PRUNE1/ARHGEF2/TPR/CAMSAP2/CCSAP/HNRNPU/MAPRE3/SPAST/DCTN1/CHMP3/CLASP1/TRAF3IP1/CLASP2/RHOA/PARP3/ATXN7/CHMP2B/CEP97/PHLDB2/GSK3B/CEP70/MAP6D1/TACC3/HAUS3/RNF4/SLAIN2/SNCA/TPPP/PRKAA1/MAP1B/EFNA5/APC/TRIM36/ATAT1/HSPA1A/HSPA1B/SENP6/RAC1/GNAI1/AKAP9/MET/CHMP7/CHMP4C/MAPK15/MPDZ/HAUS6/CHMP5/GBA2/BICD2/CDK5RAP2/ABL1/CAMSAP1/KIF18A/CKAP5/EML3/MARK2/ARL2/CDK2AP2/NUMA1/RPS3/PAK1/DIXDC1/PHLDB1/FKBP4/CDKN1B/BICD1/NAV3/CLIP1/SKA3/CENPJ/CKAP2/BORA/ARHGEF7/HAUS4/CHMP4A/TOGARAM1/CHMP4BP1/DYNC1H1/HAUS2/TTBK2/MAP1A/CIB1/PKD1/BMERB1/PLK1/CYLD/KATNB1/CDH5/CHMP1A/PAFAH1B1/RANGRF/SPAG5/TAOK1/GIT1/CDK5R1/MAPT/SKA2/CLTC/CHMP6/TBCD/CHMP1B/ROCK1/MAPRE2/HAUS1/SKA1/VPS4B/APC2/CAMSAP3/HAUS8/MAP1S/HAUS5/CLIP3/EML2/NUP62/CHMP2A/TPX2/MAPRE1/CHMP4B/RAE1/DYRK1A/GAS2L1/DRG1/MID1/MID1IP1/HDAC6/HAUS7/MECP2
GO:0044380	protein localization to cytoskeleton	BP	BP	57/11067		1.79754256117842e-11	3.25844958881127e-10			DVL1/KLHL21/STIL/CEP350/DISC1/HNRNPU/MAPRE3/CRIPT/GSK3B/GOLGB1/CCDC14/CEP72/APC/DIAPH1/TTK/SNX10/NUDCD3/MCPH1/PCM1/HOOK3/UBXN2B/FAM83H/ABHD17B/ABL1/KIF20B/NUMA1/C2CD3/BICD1/DCTN2/CEP83/PIBF1/CHAMP1/TTBK2/MAP1A/RAB11A/BBS4/ABHD17C/RAB11FIP3/PARD6A/KIAA0753/SPAG5/PPP1R9B/CEP131/CSNK1D/CEP192/MAPRE2/ABHD17A/MARK4/NUP62/NSFL1C/MAPRE1/CEP250/FAM83D/AURKA/GAS2L1/MID1/MID2
GO:0051495	positive regulation of cytoskeleton organization	BP	BP	136/11067		1.03453573595148e-05	6.99037068351711e-05			MTOR/ARHGEF10L/CDC42/WASF2/STIL/SASS6/GPSM2/PSRC1/RHOC/PDE4DIP/S100A10/NES/KIRREL1/PFDN2/ITGB1BP1/ROCK2/SPAST/CDC42EP3/PRKCE/CCDC88A/PLEK/DCTN1/NCK2/CLASP1/BIN1/NCKAP1/ABI2/ARPC2/BRK1/RHOA/CD47/NCK1/PFN2/DLG1/WDR1/LIMCH1/SLAIN2/CRACD/PLK4/RICTOR/MAP1B/F2RL1/FER/CEP120/FCHSD1/SYNPO/EDN1/CARMIL1/TRIM27/HSPA1A/HSPA1B/WASF1/CCN2/SNX9/RAC1/LIMK1/AKAP9/BAIAP2L1/PPP1R35/MET/BRAF/EPHA1/ARHGEF5/ARHGEF10/SORBS3/PTK2B/BAG4/MTSS1/MAPK15/TESK1/TGFBR1/CDK5RAP2/GSN/ABL1/NRP1/WASHC2C/ADD3/SWAP70/CKAP5/ARL2/CTTN/NUMA1/FCHSD2/RPS3/WNT11/PAK1/CEP295/CDKN1B/RAPGEF3/NAV3/PXN/CLIP1/CENPJ/CFL2/TOGARAM1/ARF6/FERMT2/TGFB3/EVL/DYNC1H1/CYFIP1/KATNBL1/C15orf62/TPM1/SMAD3/WHAMM/MLST8/MYLK3/KATNB1/FHOD1/CARMIL2/SERPINF2/PFN1/SPAG5/GIT1/CDK5R1/MAPT/CDC42EP4/GRB2/BAIAP2/VPS4B/NPHS1/VASP/NUP62/DSTN/MAPRE1/SDC4/PPM1F/NF2/DRG1/CDC42EP1/PDXP/BAIAP2L2/MECP2/FLNA/PLXNA3
GO:0010631	epithelial cell migration	BP	BP	221/11067		0.4033733388851229	0.5348707022067942			PLEKHG5/PIK3CD/MTOR/EPHA2/ZC3H12A/MACF1/EDN2/SVBP/PIK3R3/PLPP3/GADD45A/PKN2/S100A2/RAB13/EFNA1/GLUL/PTGS2/ADIPOR1/ATP2B4/TGFB2/DUSP10/MIA3/LGALS8/ITGB1BP1/ADAM17/ROCK2/RHOB/CYP1B1/PRKCE/RTN4/WDPCP/ATOH8/MAP4K4/EPB41L5/CLASP1/ZEB2/NFE2L2/BMPR2/NRP2/AAMP/SCG2/SP100/VHL/PPARG/IQSEC1/CAPN7/TGFBR2/CLASP2/PTPN23/GPX1/RHOA/HYAL1/WNT5A/FOXP1/ROBO1/FSTL1/GATA2/PLXND1/PIK3CB/PFN2/PDCD10/PIK3CA/S100P/FGFBP1/ANXA3/EGF/FGF2/FBXW7/PDCD6/ITGA2/PLK2/ARSB/MACIR/MCC/HBEGF/SPARC/FGF18/RREB1/EDN1/GPLD1/CSNK2B/PPARD/SRF/VEGFA/NUS1/SASH1/RAC1/ANLN/HSPB1/KRIT1/EPHB4/MET/PAXIP1/EGR3/LOXL2/DOCK5/PTK2B/ADGRA2/FGFR1/ADAM9/SNAI2/ANGPT1/CCN3/HAS2/PTK2/PTP4A3/GFUS/EPPK1/KANK1/TESK1/ANXA1/TGFBR1/KLF4/EPB41L4B/DAB2IP/PKN3/ABL1/NOTCH1/GATA3/ITGB1/NRP1/SIRT1/MMRN2/PTEN/NANOS1/DOCK1/PIK3C2A/LPXN/CORO1B/PRCP/ETS1/HDAC7/ACVRL1/NR4A1/SP1/ATP5F1B/KITLG/DCN/CORO1C/PTPN11/PXN/P2RX4/SCARB1/HMGB1/STARD13/IRS2/LTB4R2/ARHGAP5/ARF6/HIF1A/SYNJ2BP/LGMN/EVL/AKT1/SPRED1/THBS1/DLL4/FGF7/RAB11A/MAP2K5/CTSH/CIB1/NR2F2/PDPK1/EMP2/CDH5/BCAR1/PLCG2/FOXC2/SERPINF1/PFN1/MAP2K3/NF1/KRT16/JUP/STAT5A/HDAC5/GRN/ITGB3/ITGA3/BCAS3/MAP3K3/PRKCA/PTPRM/ROCK1/MAPRE2/ATP5F1A/SMAD4/TBXA2R/LRG1/KANK2/CALR/PKN1/GIPC1/GPI/TGFB1/APOE/PRKD2/FUT1/RRAS/EMC10/ZNF580/FERMT1/RIN2/ID1/SRC/PLCG1/SNAI1/SOX18/PPM1F/PATZ1/HMOX1/MYH9/CARD10/SH3BP1/PDGFB/PRKX/TMSB4X/HDAC6/SRPX2/MECP2
GO:0090130	tissue migration	BP	BP	221/11067		0.5993037755579282	0.6918332453304606			PLEKHG5/PIK3CD/MTOR/EPHA2/ZC3H12A/MACF1/EDN2/SVBP/PIK3R3/PLPP3/GADD45A/PKN2/S100A2/RAB13/EFNA1/GLUL/PTGS2/ADIPOR1/ATP2B4/TGFB2/DUSP10/MIA3/LGALS8/ITGB1BP1/ADAM17/ROCK2/RHOB/CYP1B1/PRKCE/RTN4/WDPCP/ATOH8/MAP4K4/EPB41L5/CLASP1/ZEB2/NFE2L2/BMPR2/NRP2/AAMP/SCG2/SP100/VHL/PPARG/IQSEC1/CAPN7/TGFBR2/CLASP2/PTPN23/GPX1/RHOA/HYAL1/WNT5A/FOXP1/ROBO1/FSTL1/GATA2/PLXND1/PIK3CB/PFN2/PDCD10/PIK3CA/S100P/FGFBP1/ANXA3/EGF/FGF2/FBXW7/PDCD6/ITGA2/PLK2/ARSB/MACIR/MCC/HBEGF/SPARC/FGF18/RREB1/EDN1/GPLD1/CSNK2B/PPARD/SRF/VEGFA/NUS1/SASH1/RAC1/ANLN/HSPB1/KRIT1/EPHB4/MET/PAXIP1/EGR3/LOXL2/DOCK5/PTK2B/ADGRA2/FGFR1/ADAM9/SNAI2/ANGPT1/CCN3/HAS2/PTK2/PTP4A3/GFUS/EPPK1/KANK1/TESK1/ANXA1/TGFBR1/KLF4/EPB41L4B/DAB2IP/PKN3/ABL1/NOTCH1/GATA3/ITGB1/NRP1/SIRT1/MMRN2/PTEN/NANOS1/DOCK1/PIK3C2A/LPXN/CORO1B/PRCP/ETS1/HDAC7/ACVRL1/NR4A1/SP1/ATP5F1B/KITLG/DCN/CORO1C/PTPN11/PXN/P2RX4/SCARB1/HMGB1/STARD13/IRS2/LTB4R2/ARHGAP5/ARF6/HIF1A/SYNJ2BP/LGMN/EVL/AKT1/SPRED1/THBS1/DLL4/FGF7/RAB11A/MAP2K5/CTSH/CIB1/NR2F2/PDPK1/EMP2/CDH5/BCAR1/PLCG2/FOXC2/SERPINF1/PFN1/MAP2K3/NF1/KRT16/JUP/STAT5A/HDAC5/GRN/ITGB3/ITGA3/BCAS3/MAP3K3/PRKCA/PTPRM/ROCK1/MAPRE2/ATP5F1A/SMAD4/TBXA2R/LRG1/KANK2/CALR/PKN1/GIPC1/GPI/TGFB1/APOE/PRKD2/FUT1/RRAS/EMC10/ZNF580/FERMT1/RIN2/ID1/SRC/PLCG1/SNAI1/SOX18/PPM1F/PATZ1/HMOX1/MYH9/CARD10/SH3BP1/PDGFB/PRKX/TMSB4X/HDAC6/SRPX2/MECP2
GO:0010632	regulation of epithelial cell migration	BP	BP	165/11067		0.8448074121030455	0.7084734281 15887			PIK3CD/MTOR/EPHA2/ZC3H12A/MACF1/SVBP/PLPP3/GADD45A/EFNA1/GLUL/PTGS2/ADIPOR1/ATP2B4/TGFB2/DUSP10/ITGB1BP1/ADAM17/ROCK2/RHOB/PRKCE/RTN4/ATOH8/MAP4K4/EPB41L5/CLASP1/NFE2L2/BMPR2/NRP2/AAMP/SP100/PPARG/IQSEC1/CAPN7/TGFBR2/CLASP2/PTPN23/RHOA/HYAL1/WNT5A/FOXP1/GATA2/PIK3CB/PFN2/PDCD10/FGFBP1/ANXA3/EGF/FGF2/FBXW7/PDCD6/ITGA2/PLK2/ARSB/MACIR/MCC/HBEGF/SPARC/FGF18/RREB1/EDN1/GPLD1/CSNK2B/VEGFA/NUS1/SASH1/RAC1/HSPB1/KRIT1/MET/DOCK5/PTK2B/ADGRA2/FGFR1/ADAM9/ANGPT1/HAS2/PTK2/GFUS/EPPK1/ANXA1/KLF4/EPB41L4B/DAB2IP/ABL1/NOTCH1/GATA3/NRP1/SIRT1/MMRN2/PTEN/DOCK1/PIK3C2A/PRCP/ETS1/HDAC7/ACVRL1/SP1/ATP5F1B/DCN/CORO1C/P2RX4/SCARB1/HMGB1/STARD13/IRS2/ARHGAP5/ARF6/HIF1A/SYNJ2BP/LGMN/EVL/AKT1/SPRED1/THBS1/DLL4/FGF7/RAB11A/MAP2K5/CTSH/CIB1/NR2F2/PDPK1/EMP2/BCAR1/PLCG2/FOXC2/SERPINF1/PFN1/MAP2K3/NF1/JUP/STAT5A/HDAC5/GRN/ITGB3/ITGA3/BCAS3/MAP3K3/PRKCA/PTPRM/MAPRE2/ATP5F1A/TBXA2R/CALR/GPI/TGFB1/APOE/PRKD2/FUT1/RRAS/EMC10/ZNF580/RIN2/SRC/PLCG1/PPM1F/PATZ1/HMOX1/CARD10/SH3BP1/PDGFB/TMSB4X/HDAC6/SRPX2/MECP2
GO:0044331	cell-cell adhesion mediated by cadherin	BP	BP	21/11067		0.9870414664 07548	0.7084734281 15887			MAD2L2/PTPRU/WNT5A/DENND6A/CDH10/FER/BMP6/FLOT1/VEGFA/AFDN/NOTCH1/PLEKHA7/CTNND1/CDH24/FOXA1/TJP1/CDH5/CDH1/SERPINF2/MMP24/PPM1F
GO:0043534	blood vessel endothelial cell migration	BP	BP	88/11067		0.9975110087 76293	0.7084734281 15887			EPHA2/PIK3R3/GADD45A/EFNA1/PTGS2/ATP2B4/MIA3/ITGB1BP1/ADAM17/CYP1B1/NFE2L2/VHL/PPARG/GPX1/RHOA/ROBO1/GATA2/PDCD10/FGFBP1/FGF2/FBXW7/PLK2/FGF18/GPLD1/CSNK2B/SRF/VEGFA/NUS1/HSPB1/EPHB4/EGR3/PTK2B/FGFR1/ANGPT1/ANXA1/KLF4/ABL1/NOTCH1/ITGB1/NRP1/SIRT1/MMRN2/PIK3C2A/PRCP/ETS1/HDAC7/ACVRL1/NR4A1/SP1/ATP5F1B/P2RX4/SCARB1/HMGB1/STARD13/HIF1A/AKT1/SPRED1/THBS1/DLL4/MAP2K5/CIB1/PDPK1/EMP2/CDH5/FOXC2/MAP2K3/NF1/JUP/STAT5A/HDAC5/MAP3K3/PRKCA/ATP5F1A/TBXA2R/TGFB1/APOE/PRKD2/ID1/PLCG1/SOX18/HMOX1/MYH9/CARD10/SH3BP1/PDGFB/TMSB4X/SRPX2/MECP2
GO:0060326	cell chemotaxis	BP	BP	142/11067		0.9999999837 19981	0.7084734281 15887			ARHGEF16/PLEKHG5/PIK3CD/EPHA2/NBL1/AKIRIN1/EDN2/PDE4B/VAV3/PIP5K1A/S100A14/RAB13/IL6R/TGFB2/LYST/ADAM17/CXCR4/PIKFYVE/SCG2/CCL20/PRSS56/ACKR3/IL17RC/OXSR1/CCR3/PRKCD/WNT5A/CXCL8/PF4V1/PF4/PPBP/CXCL5/CXCL3/CXCL2/FGF2/GAB1/HMGB2/ITGA1/F2RL1/LOX/SLC12A2/HBEGF/CSF1R/PDGFRB/CD74/FGF18/DUSP1/NEDD9/EDN1/VEGFA/TPBG/RAC1/IL6/PPIA/SBDS/HSPB1/SERPINE1/DOCK4/MET/ARHGEF5/MTUS1/EGR3/PTK2B/FGFR1/LYN/CCN3/PTK2/PLEC/CREB3/ANXA1/NINJ1/C5/NOTCH1/CAMK1D/NRP1/MCU/GBF1/ADAM8/RHOG/SWAP70/PARVA/MDK/VEGFB/CORO1B/TIRAP/WNK1/DNM1L/ANO6/BIN2/NR4A1/SLC8B1/P2RX4/HMGB1/GAS6/SRP54/LGALS3/LGMN/THBS1/ADAM10/DAPK2/PPIB/ABCC1/MAPK3/HSD3B7/BCAR1/CRK/ARRB2/C1QBP/TMEM102/LGALS9/CCL2/MMP28/CCL5/NUP85/RAC3/TNFRSF11A/BSG/PIP5K1C/VAV1/CALR/ADGRE2/RPS19/PRKD2/C5AR1/C5AR2/TRPM4/RPL13A/ZNF580/ELMO2/PREX1/CXADR/TRPM2/ITGB2/IL17RA/CRKL/MAPK1/DDT/PDGFB/TMSB4X/MOSPD2/PLXNB3/MPP1

Supplementary Table 1 | GO Enrichment Analysis of L-MAT-induced HeLa Cells, related to Figure 3F.

Supplementary Table 2: Differentially Expressed Genes in Enriched Pathways (related to Figure 3G)

Gene Symbol	Gene Name	log_2FC	p-value	Associated GO Terms
RHOA	RHOA	-0.0110	3.70e-11	regulation of microtubule cytoskeleton organization
RAC1	RAC1	0.1853	3.70e-11	regulation of microtubule cytoskeleton organization
MET	MET	-0.2105	3.70e-11	regulation of microtubule cytoskeleton organization
ABL1	ABL1	0.2590	3.70e-11	regulation of microtubule cytoskeleton organization
MECP2	MECP2	-0.1367	3.70e-11	regulation of microtubule cytoskeleton organization
ABL1	ABL1	0.2590	4.60e-10	protein localization to cytoskeleton
RHOA	RHOA	-0.0110	9.87e-05	positive regulation of cytoskeleton organization
RAC1	RAC1	0.1853	9.87e-05	positive regulation of cytoskeleton organization
MET	MET	-0.2105	9.87e-05	positive regulation of cytoskeleton organization
PTK2B	PTK2B	-0.4332	9.87e-05	positive regulation of cytoskeleton organization
ABL1	ABL1	0.2590	9.87e-05	positive regulation of cytoskeleton organization
NRP1	NRP1	-0.2914	9.87e-05	positive regulation of cytoskeleton organization
MECP2	MECP2	-0.1367	9.87e-05	positive regulation of cytoskeleton organization
ADAM17	ADAM17	0.3796	0.755	epithelial cell migration
RHOA	RHOA	-0.0110	0.755	epithelial cell migration
VEGFA	VEGFA	1.1989	0.755	epithelial cell migration
RAC1	RAC1	0.1853	0.755	epithelial cell migration
MET	MET	-0.2105	0.755	epithelial cell migration
PTK2B	PTK2B	-0.4332	0.755	epithelial cell migration
ABL1	ABL1	0.2590	0.755	epithelial cell migration
NOTCH1	NOTCH1	0.1728	0.755	epithelial cell migration
NRP1	NRP1	-0.2914	0.755	epithelial cell migration
MECP2	MECP2	-0.1367	0.755	epithelial cell migration
ADAM17	ADAM17	0.3796	0.977	tissue migration
RHOA	RHOA	-0.0110	0.977	tissue migration
VEGFA	VEGFA	1.1989	0.977	tissue migration
RAC1	RAC1	0.1853	0.977	tissue migration
MET	MET	-0.2105	0.977	tissue migration
PTK2B	PTK2B	-0.4332	0.977	tissue migration
ABL1	ABL1	0.2590	0.977	tissue migration
NOTCH1	NOTCH1	0.1728	0.977	tissue migration
NRP1	NRP1	-0.2914	0.977	tissue migration
MECP2	MECP2	-0.1367	0.977	tissue migration
ADAM17	ADAM17	0.3796	1.000	regulation of epithelial cell migration
RHOA	RHOA	-0.0110	1.000	regulation of epithelial cell migration
VEGFA	VEGFA	1.1989	1.000	regulation of epithelial cell migration
RAC1	RAC1	0.1853	1.000	regulation of epithelial cell migration
MET	MET	-0.2105	1.000	regulation of epithelial cell migration
PTK2B	PTK2B	-0.4332	1.000	regulation of epithelial cell migration
ABL1	ABL1	0.2590	1.000	regulation of epithelial cell migration
NOTCH1	NOTCH1	0.1728	1.000	regulation of epithelial cell migration
NRP1	NRP1	-0.2914	1.000	regulation of epithelial cell migration
MECP2	MECP2	-0.1367	1.000	regulation of epithelial cell migration
VEGFA	VEGFA	1.1989	1.000	cell-cell adhesion mediated by cadherin
NOTCH1	NOTCH1	0.1728	1.000	cell-cell adhesion mediated by cadherin
ADAM17	ADAM17	0.3796	1.000	blood vessel endothelial cell migration
RHOA	RHOA	-0.0110	1.000	blood vessel endothelial cell migration
VEGFA	VEGFA	1.1989	1.000	blood vessel endothelial cell migration
PTK2B	PTK2B	-0.4332	1.000	blood vessel endothelial cell migration
ABL1	ABL1	0.2590	1.000	blood vessel endothelial cell migration
NOTCH1	NOTCH1	0.1728	1.000	blood vessel endothelial cell migration
NRP1	NRP1	-0.2914	1.000	blood vessel endothelial cell migration
MECP2	MECP2	-0.1367	1.000	blood vessel endothelial cell migration
ADAM17	ADAM17	0.3796	1.000	cell chemotaxis
VEGFA	VEGFA	1.1989	1.000	cell chemotaxis
RAC1	RAC1	0.1853	1.000	cell chemotaxis
MET	MET	-0.2105	1.000	cell chemotaxis
PTK2B	PTK2B	-0.4332	1.000	cell chemotaxis
NOTCH1	NOTCH1	0.1728	1.000	cell chemotaxis
NRP1	NRP1	-0.2914	1.000	cell chemotaxis

Supplementary Table 2 | Differentially Expressed Genes in Enriched Pathways, related to Figure 3G.

Supplementary Table 3: Analysis Parameters and Software (related to Figure 1C and supplementary Figure 2B)

Parameter	Value/Setting
Analysis software	DESeq2
R version	4.3.1
Organism database	hg38
Background gene set	All expressed genes after filtering
Statistical test	Wald test (negative binomial model)
Multiple testing correction	Benjamini–Hochberg (BH)
p-value cutoff	0.05
FDR cutoff	0.05
Minimum gene count	≥10 reads across three samples
Visualization package	ggplot2 (with ggrepel, dplyr)

Supplementary Table 3 | Analysis Parameters and Software1222, related to Figure 1C and Supplementary Figure 2B.